J. Fluid Mech. (2008), *vol.* 617, *pp.* 107–140. © 2008 Cambridge University Press
doi:10.1017/S0022112008003637 Printed in the United Kingdom

Mean momentum balance in moderately favourable pressure gradient turbulent boundary layers

M. METZGER[1], A. LYONS[1] AND P. FIFE[2]

[1]Department of Mechanical Engineering, University of Utah, Salt Lake City, UT 84112, USA
[2]Department of Mathematics, University of Utah, Salt Lake City, UT 84112, USA

(Received 7 June 2007 and in revised form 4 August 2008)

Moderately favourable pressure gradient turbulent boundary layers are investigated within a theoretical framework based on the unintegrated two-dimensional mean momentum equation. The present theory stems from an observed exchange of balance between terms in the mean momentum equation across different regions of the boundary layer. This exchange of balance leads to the identification of distinct physical layers, unambiguously defined by the predominant mean dynamics active in each layer. Scaling domains congruent with the physical layers are obtained from a multi-scale analysis of the mean momentum equation. Scaling behaviours predicted by the present theory are evaluated using direct measurements of all of the terms in the mean momentum balance for the case of a sink-flow pressure gradient generated in a wind tunnel with a long development length. Measurements also captured the evolution of the turbulent boundary layers from a non-equilibrium state near the wind tunnel entrance towards an equilibrium state further downstream. Salient features of the present multi-scale theory were reproduced in all the experimental data. Under equilibrium conditions, a universal function was found to describe the decay of the Reynolds stress profile in the outer region of the boundary layer. Non-equilibrium effects appeared to be manifest primarily in the outer region, whereas differences in the inner region were attributed solely to Reynolds number effects.

1. Introduction

Several theoretical approaches for deriving scaling relations in wall-bounded turbulent flows have been pursued in the literature, including those of, among others, Yaglom (1979), Long & Chen (1981), Panton (1990), Durbin & Belcher (1992), Barenblatt, Chorin & Prostokishin (1997), Sreenivasan & Sahay (1997), George & Castillo (1997), Wosnik, Castillo & George (2000) and Perry, Marusic & Jones (2002). Until recently (Fife *et al.* 2005*b*; Wei *et al.* 2005*a*), none of the previous theories utilized a straightforward comparison of the relative magnitude of the forces in the unintegrated mean momentum balance as a function of distance from the wall. By doing so, Wei *et al.* (2005*a*) presented a new four-layer model for fully developed two-dimensional turbulent channel flow (henceforth referred to simply as channel flow), based on an exchange of balance between the various terms in the mean momentum balance, which represent forces due to viscosity, turbulence and imposed pressure gradient. Observations from available experimental and numerical data showed that usually only two of the three forces are dominant in any given region of the boundary layer. This led to the identification of distinct physical layers, defined according to the predominant mean dynamics active in that region. In addition to their empirical observations, Wei *et al.* (2005*a*) also provided new insight into wall-flow structure based on a multi-scale mathematical analysis of the mean momentum balance. From this, Fife *et al.* (2005*a*, *b*) developed a systematic 'scaling patch' approach for determining the local scaling properties of mean profiles, which differs in important ways from approaches based on classical overlap arguments (see e.g. Millikan 1939).

Because the multi-scale theory of Fife *et al.* (2005*a*, *b*) and Wei *et al.* (2005*a*) is derived directly from the equations governing the mean dynamics of the flow (with reasonable assumptions designed to fill the gaps created by the averaging process), it has the potential to provide a consistent framework for investigating scaling behaviours in both canonical and non-canonical wall-bounded flows. The present study represents the first step towards accessing this potential by examining whether the multi-scale approach extends in a straightforward manner to moderately favourable pressure gradient (FPG) turbulent boundary layers (TBLs). Here, 'moderately' implies that the flow does not approach the relaminarization state. The FPG TBL was chosen because it is perhaps one of the least complicated (both experimentally and numerically) non-canonical wall-bounded flows to study. Other non-canonical wall-bounded flows, such as adverse pressure gradient or separating TBLs, have a tendency to exhibit three-dimensional effects (Clauser 1954; Piquet 2001). A prototypical example of an FPG TBL is the flow through a wedge driven by a potential sink of momentum located at the vertex of the wedge. The potential sink causes the flow to accelerate through the wedge, thereby producing an FPG in the streamwise direction. The flow in the immediate vicinity of the lower – and upper – plates is typically referred to as a sink-flow TBL. The interesting feature of the sink-flow TBL relates to its unique property of attaining precise equilibrium (described further in § 1.1) sufficiently near the sink singularity (Coles 1957; Rotta 1962). The similarity relations valid under equilibrium conditions make the present theoretical analysis simpler and more complete. Importantly though, the bulk of the theory presented herein does not necessarily require the flow to be in equilibrium, nor does the theory depend on the particular form of the applied FPG, and therefore it is not limited exclusively to sink-flow TBLs.

There are three main aims of the present study. One is to examine similarities and differences between the FPG TBL and the channel flow with regard to the mathematical formulation of the multi-scale analysis. Because of the formal analogies in the two cases, very similar methods can be used and conclusions reached. Secondly, experimental data by the authors are used to observe the exchange of balance between terms in the mean momentum equation and subsequent scaling properties of the mean profiles. Finally, the concept of equilibrium is explored by looking at the response of the terms in the mean momentum balance, as the TBL progresses towards an equilibrium state. The paper is outlined as follows: First, a brief review of equilibrium boundary layers is given in § 1.1. The properties of sink flow are described in § 1.2. The experimental facility and techniques are specified in § 2. The mathematical formulation of the present theory is developed in § 3, an important aspect of which is modelling the mean advection inside the boundary layer as a natural extension of the potential flow advection at the edge of the boundary layer. Section 4 describes the physical layer structure and scaling patch analysis as governed by the particular force balances operating at different locations in the flow domain. Experimental results are then presented in § 5, demonstrating both non-equilibrium and Reynolds number effects.

1.1. *Equilibrium boundary layers*

The equilibrium layer was first identified as an important class of TBLs in the 1950s and 1960s (Clauser 1954, 1956; Townsend 1956; Coles 1957; Townsend 1961; Rotta 1962; Bradshaw 1967). This section describes equilibrium layers from the context of self-preserving flow, analogous to the laminar boundary layers studied by Falkner & Skan (1931) and provides a brief background of the various criteria in the literature used to identify equilibrium layers. In a self-preserving flow, the governing equations may be recast as non-dimensional ordinary differential equations through the proper choice of length ($\tilde{\ell}$) and velocity ($\tilde{u}$) scales. Townsend (1956) and Rotta (1962) outline this procedure for the mean flow in a two-dimensional TBL. This procedure assumes similarity of the velocity defect and Reynolds shear stress profiles, using a single characteristic velocity scale, of the form

$$U_o - U = \tilde{u}\, f(\eta), \tag{1.1}$$

$$\langle uv \rangle = \tilde{u}^2\, g(\eta), \tag{1.2}$$

where $\eta = y/\tilde{\ell}$ represents the non-dimensional wall-normal coordinate; U and U_o represent the mean velocity inside the boundary layer and free stream velocity, respectively, and $\tilde{\ell}$ and $\tilde{u}$ are functions of the streamwise coordinate x only. Substituting these relations into the mean momentum balance and combining with the continuity equation to eliminate the vertical velocity, one obtains

$$\begin{aligned} -\left[\frac{\tilde{\ell}}{\tilde{u}}\frac{\mathrm{d}U_o}{\mathrm{d}x}\right] f - \left[\frac{U_o\tilde{\ell}}{\tilde{u}^2}\frac{\mathrm{d}\tilde{u}}{\mathrm{d}x}\right] f + \left[\frac{\tilde{\ell}}{\tilde{u}}\frac{\mathrm{d}\tilde{u}}{\mathrm{d}x}\right] f^2 + \left[\frac{U_o}{\tilde{u}}\frac{\mathrm{d}\tilde{\ell}}{\mathrm{d}x}\right] \eta f' + \left[\frac{\tilde{\ell}}{\tilde{u}}\frac{\mathrm{d}U_o}{\mathrm{d}x}\right] \eta f' \\ - \left[\frac{\tilde{\ell}}{\tilde{u}}\frac{\mathrm{d}\tilde{u}}{\mathrm{d}x}\right] f' \int_0^1 f\, \mathrm{d}\eta - \left[\frac{\mathrm{d}\tilde{\ell}}{\mathrm{d}x}\right] f' \int_0^1 f\, \mathrm{d}\eta + g' + \left[\frac{\nu}{\tilde{\ell}\tilde{u}}\right] f'' = 0. \end{aligned} \tag{1.3}$$

Details of this operation may be found in Lyons (2007). In order for (1.3) to be an ordinary differential equation with independent variable η, each coefficient in square brackets must be constant (i.e. independent of x). On the basis of this, it follows (Townsend 1956, 1961; Rotta 1962) that the requirements for self-preserving flow, assuming a single characteristic velocity scale, are

$$\mathrm{d}\tilde{\ell}/\mathrm{d}x = \text{constant}, \tag{1.4}$$

$$\tilde{u}/U_o = \text{constant}, \tag{1.5}$$

$$(\tilde{\ell}/\tilde{u})(\mathrm{d}\tilde{u}/\mathrm{d}x) = \text{constant}. \tag{1.6}$$

Relation (1.4) requires that the characteristic length scale vary linearly with downstream distance x. A channel with the upper and lower walls diverging or converging at a constant angle is one means of obtaining this criterion. The sink flow, described in more detail in § 1.2, represents the latter case. However, other geometries may also be used (see e.g. Skare & Krogstad 1994).

Combining (1.5) and (1.6), along with the inviscid flow relation $\rho\, U_o(\mathrm{d}U_o/\mathrm{d}x) = -\,\mathrm{d}p/\mathrm{d}x$, one obtains the criterion

$$\frac{\delta}{\tau_w}\frac{\mathrm{d}p}{\mathrm{d}x} = \text{constant}, \tag{1.7}$$

where the local boundary layer thickness and friction velocity have been used, for example, as the characteristic length and velocity scales, i.e. $\tilde{\ell} \equiv \delta$ and $\tilde{u} \equiv u_\tau$, where $u_\tau = \sqrt{\tau_w/\rho}$ with ρ and τ_w denoting the fluid density and wall shear stress, respectively. Note that (1.7) is identical to the criterion for self-preserving laminar boundary layers of the type studied by Falkner & Skan (1931). Furthermore, Clauser (1954) stated that a boundary layer will have a constant history and, thus, be classified as an 'equilibrium' flow if (1.7) is satisfied, except that Clauser (1954) utilized $\tilde{\ell} \equiv \delta'$, where δ' denotes an effective boundary layer thickness that was never explicitly defined.

In contrast to (1.1), Coles (1957) writes the general form of the velocity defect law as $U_o - U = u_\tau\, F(\pi, \eta)$, where π represents a measure of the relative magnitude of the wake and wall components of the flow. The criterion that Coles (1957) uses to define an equilibrium boundary is that π remain independent of x, resulting in a velocity defect independent of x outside of the sub-layer. Coles (1957) concludes, based in part on experimental data and the analogy with laminar flow, that this criterion is satisfied for equilibrium TBLs when

$$D \equiv \frac{u_\tau}{U_o} \frac{(\partial U_o/\partial x)}{(\partial u_\tau/\partial x)} = \text{constant}. \tag{1.8}$$

The criterion $D = \text{constant}$ can be derived directly from the self-preserving form of the mean momentum equation by again combining (1.5) and (1.6) and using $\tilde{u} \equiv u_\tau$.

Bradshaw (1967) indicates that a necessary condition for similarity of the velocity defect profile is that the contribution of the pressure gradient to the growth of the momentum deficit remain constant, resulting in the condition that

$$\beta \equiv \frac{\delta_1}{\tau_w} \frac{\mathrm{d}p}{\mathrm{d}x} = \text{constant}, \tag{1.9}$$

where δ_1 denotes the displacement thickness. This condition is consistent with (1.7), as explained in the following. Assuming similarity of the velocity defect profile (1.1) with $\tilde{u} \equiv u_\tau$, the displacement thickness may be written as

$$\delta_1 = \frac{u_\tau\, \delta}{U_o} \int_0^1 f\, \mathrm{d}\eta. \tag{1.10}$$

Substituting (1.10) into (1.7) and using the criterion (1.5) leads directly to the result that $\beta = \text{constant}$ for an equilibrium layer.

Castillo & George (2001) define an equilibrium boundary layer as one in which the pressure gradient parameter Λ remains constant, i.e.

$$\Lambda \equiv \frac{\delta}{\rho U_o^2 (\mathrm{d}\delta/\mathrm{d}x)} \frac{\mathrm{d}p}{\mathrm{d}x} = \text{constant}. \tag{1.11}$$

This criterion also follows directly from the self-preserving form of the mean momentum equation by combining (1.4)–(1.6), along with the inviscid relation $\rho\, U_o(\mathrm{d}U_o/\mathrm{d}x) = -\mathrm{d}p/\mathrm{d}x$, and taking $\tilde{\ell} \equiv \delta$.

Contrary to the studies described above, Townsend (1956, 1961) defines an equilibrium layer as a region (relatively small compared to the thickness of the boundary layer) wherein production of turbulent kinetic energy approximately balances dissipation and advection terms remain negligible. In this sense, 'equilibrium' layer refers to energy equilibrium. For a boundary layer having a region adjacent to the wall with nearly constant shear stress, Townsend (1961) shows that the criterion for energy equilibrium in that region leads to the well-known log law behaviour of the inner normalized mean velocity profile in the region. As such, the flow may be considered self-preserving in the small region of the boundary layer, satisfying energy equilibrium, regardless of the self-preserving nature of the outer flow. In the present study, however, the term 'equilibrium layer' refers to the situation in which the entire boundary layer (excluding the viscous sub-layer) achieves an approximate

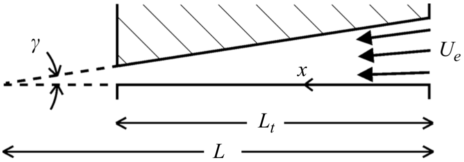

FIGURE 1. Flow through a wedge driven by a potential sink of momentum located at $x = L$. In the experiments, a fan located at $x = L_t$ simulates the effect of a virtual momentum sink.

self-preserving state, such that the flow satisfies two or more of the criteria (1.4)–(1.6) necessary to obtain the self-preserving form of the mean momentum balance, assuming similarity of the velocity defect and Reynolds stress profiles. This definition of equilibrium is preferred here because, although more restrictive compared to Townsend's view, it represents the condition wherein the entire boundary layer loses memory of its upstream history.

1.2. *Sink flow*

The mathematical analysis presented herein is motivated and evaluated using experimental data by the authors from both equilibrium and non-equilibrium sink-flow TBLs, in addition to available data from direct numerical simulations (DNS) of equilibrium sink-flow TBLs (Spalart 1986). Here, 'non-equilibrium' refers to the state of the flow in the entrance region of the experimental facility; as the flow progresses downstream, it eventually loses all memory of its upstream history, thus attaining equilibrium. Figure 1 illustrates the present experimental configuration used to generate a sink flow, i.e. flow through a two-dimensional wedge. (Further details of the experiments are provided in § 2.) Streamlines in the potential core of the channel (outside of the boundary layers that develop along the channel walls) are directed radially towards a virtual point sink of momentum located at $x = L$, corresponding to the vertex of the two channel walls. The strength of the virtual momentum sink is characterized by the entrance velocity U_e and height of the channel opening at $x = 0$. The angle γ is small enough to ensure that typical boundary layer assumptions remain valid. The sink-flow TBL was chosen for comparison with the present theory for several reasons: (i) the flow geometry is relatively simple; (ii) data from DNS (Spalart 1986) and laboratory experiments (Jones, Marusic & Perry 2001) already exist over a substantial Reynolds number range and (iii) both equilibrium and non-equilibrium conditions are achievable with a single flow configuration. Experimental studies (Jones *et al.* 2001) show that the sink-flow TBL attains equilibrium at a streamwise distance $x/L \approx 0.6$ from the entrance of the wedge.

From the geometry and mass conservation, it is clear that

$$U_o = U_e \left(1 - \frac{x}{L}\right)^{-1}, \tag{1.12}$$

where U_0 denotes the flow outside of the boundary layer (in the potential core of the channel). Under these conditions, the boundary layer developing along the floor is subjected to a moderately FPG, $U_o\,(\mathrm{d}U_o/\mathrm{d}x) > 0$, of the form

$$U_o\,\frac{\mathrm{d}U_o}{\mathrm{d}x} = \frac{U_e^2}{L\,(1 - x/L)^3}, \tag{1.13}$$

where Euler's equation (for inviscid flow) has been used to write the pressure gradient in terms of the mean advection *outside* the boundary layer, i.e. $-\rho^{-1}(\mathrm{d}P/\mathrm{d}x) = U_o(\mathrm{d}U_o/\mathrm{d}x)$. A non-dimensional pressure gradient or acceleration

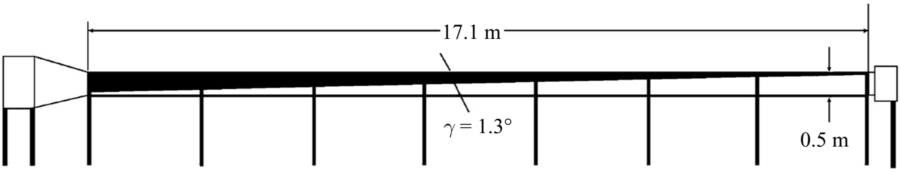

Figure 2. Schematic of wind tunnel with angled ceiling used to model a sink flow.

parameter K is introduced following convention,

$$K = -\frac{\nu}{\rho U_o^3}\frac{\mathrm{d}P}{\mathrm{d}x} = \frac{\nu}{U_o^2}\frac{\mathrm{d}U_o}{\mathrm{d}x}, \tag{1.14}$$

where ν denotes the kinematic viscosity. For the particular case of a sink flow,

$$K = \frac{\nu}{L\,U_e}, \tag{1.15}$$

which looks like an inverse Reynolds number. The coefficient of pressure is given by

$$C_p = \frac{P - P_e}{1/2\,\rho U_e^2} = 1 - \frac{1}{(1 - x/L)^2}, \tag{1.16}$$

where P_e denotes the reference static pressure at the entrance.

2. Experimental techniques

2.1. *Wind tunnel facility*

An open–return suction wind tunnel, with a long development length, served as the experimental facility. The test section of the wind tunnel measures 17.1 m long, 0.61 m wide and 0.5 m high. Flow enters the facility through a straight section containing a series of screens and honeycombs. In order to simulate sink flow, a false ceiling (made of Styrofoam panels) was prefabricated and inserted into the test section at an angle $\gamma = 1.3°$, as shown in figure 2. Lyons (2007) provides further details regarding the design of the ceiling and optimization of the slope. A trip wire of diameter d was located at the entrance of the test section ($x = 0$), such that $U_e d/\nu$ matched that prescribed by Erm & Joubert (1991). The long length of the test section allowed greater boundary layer growth, which resulted in better spatial resolution of the measurement probes compared to that offered by a shorter test section.

2.2. *Hot-wire probes*

Instantaneous horizontal (u) and vertical (v) velocities were measured using constant temperature hot-wire anemometers (AA Labs 1003), in conjunction with both normal-wire and x-array probes (manufactured in-house). The hot-wire probes consisted of a 5-μm tungsten filament, copper-plated at the ends, leaving an unplated (active) region in the centre of length $\ell_w = 1$ mm. The two tungsten filaments comprising the x-array were slanted by $\pm 45°$ and separated by $d_w = 1$ mm in the spanwise direction.

Figure 3 shows a schematic of the hot-wire configuration used in the present study. Two normal-wire probes and one x-array probe were attached to a single vertical rod and traversed simultaneously through the boundary layer, using a motorized linear slide (Velmex) positioned underneath the wind tunnel floor. The two normal-wire probes were staggered ± 152 mm in the streamwise direction, relative to the centrally located x-array, and offset by 100 mm in the spanwise direction (in order to avoid flow

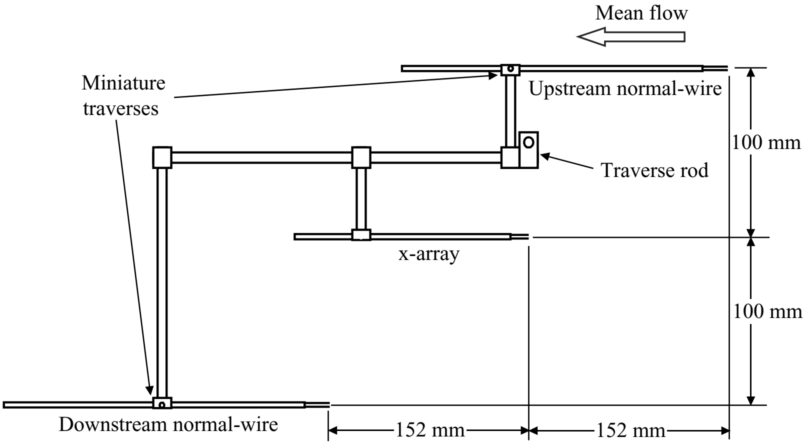

FIGURE 3. Hot-wire configuration used to simultaneously measure all of the terms in the mean momentum balance (top view).

disturbances due to the staggered streamwise arrangement). All three probes were aligned in the vertical direction with the aid of a telescope (resolution of 0.05 mm) by first fixing the position of the x-array probe and then manually adjusting two separate miniature traverses attached to the mounting stings of the two normal-wire probes. The staggered arrangement allowed direct measurement of all of the terms in the mean momentum balance; further details of the calculations are given by Lyons (2007). To verify that the flow is two-dimensional, two separate normal-wire probes were spaced approximately 250 mm apart in the spanwise direction and traversed simultaneously across the boundary layer at eight streamwise locations between $0.66 \leqslant x/L \leqslant 0.2$. The difference in the mean profiles was less than 1 %, and no distinct trends were observed as a function of x/L, indicating that the present flow could be considered two-dimensional. All hot-wire probes were calibrated in the free stream of the wind tunnel before and after each profile, using the methodology described in detail by Metzger & Klewicki (2003). The free stream velocity during calibration was measured using a Pitot-static tube (collocated with the hot-wire probes, which were adjusted to the same x position for calibration) and a high-accuracy differential pressure transducer (MKS Baratron, 1.0 mm Hg full scale).

2.3. *Experimental parameters*

Table 1 summarizes the relevant parameters in the present wind tunnel experiments, in addition to those from the DNS study of Spalart (1986). Here, the superscript + indicates inner normalization using ν and u_τ. Mean and turbulence data were obtained for entrance velocities $U_e = 1.6$ and $U_e = 2.4$ m s^{-1}, which produced moderately FPGs corresponding to $K = 5.6 \times 10^{-7}$ and 3.7×10^{-7}, respectively. The Kármán numbers (defined as $Re_\tau = \delta u_\tau/\nu$, where δ denotes the boundary layer thickness) of the combined DNS and present experimental data spanned almost an order of magnitude (i.e. $250 \leqslant Re_\tau \leqslant 1646$). Note $\delta^+ \equiv Re_\tau$. At each U_e setting, velocity profiles were obtained at $x/L = 0.29$, 0.39, 0.54, 0.66. Each profile consisted of approximately 50 wall-normal locations, spaced logarithmically from the wall. At each wall-normal location, data were sampled (using IOTech ADC488/8SA analog to digital converter) at 5 kHz over a period equal to about 10 000 times the local integral time scale, as recommended by Klewicki *et al.* (1990) in order to achieve well-converged variance and covariance statistics. The local friction velocity u_τ ($\equiv \sqrt{\tau_w/\rho}$, where τ_w represents

Available DNS data (equilibrium only)

R_θ	R_τ	K ($\times 10^7$)	U_e (m s^{-1})	ℓ_w^+, d_w^+	line
380	250	27.5	NA	∼6	· · ·
415	285	25	NA	∼6	— —
690	440	15	NA	∼6	—

Present experimental data

R_θ	R_τ	K ($\times 10^7$)	U_e (m s^{-1})	ℓ_w^+, d_w^+	x/L	symbol
884	528	5.6	1.6	5.8	0.29	
1210	724	5.6	1.6	7.4	0.39	
1587	925	5.6	1.6	9.4	0.54	
1618	1170	5.6	1.6	11.5	0.66	△
1387	790	3.7	2.4	8	0.29	*
1700	1018	3.7	2.4	10.3	0.39	◇
2033	1307	3.7	2.4	13.3	0.54	□
2443	1646	3.7	2.4	16.1	0.66	○

TABLE 1. Present experimental parameters plus those from the DNS study of Spalart (1986).

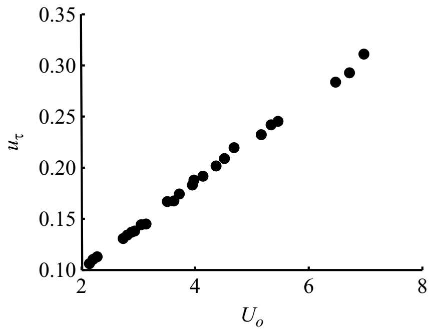

FIGURE 4. Friction velocity versus free stream velocity for all of the wind tunnel data.

the wall shear stress) associated with each profile was determined using the Clauser chart method (Clauser 1954). This method forces the logarithmic region of the inner normalized mean profile to fall along a line of constant skin friction coefficient C_f. All of the mean profiles in the present study exhibited extended logarithmic regions and hence were well suited for use with the Clauser method. Over a similar K range as investigated in the present study, Jones *et al.* (2001) found that the Clauser method (using log law constants $\kappa = 0.41$ and $A = 5.0$) overestimated u_τ by less than approximately 1.5 %, as compared to that expected from the integral momentum equation applied in the equilibrium region. Figure 4 shows a plot of u_τ as a function of U_o for all of the present wind tunnel data.

2.4. *Potential flow measurements*

Verification of the bulk flow was performed by comparing measurements of U_o and C_p with those expected from the inviscid theory for a point sink of momentum, as given by (1.12) and (1.16), respectively. The experimental values of C_p as a function of x were obtained using wall pressure taps located along the centreline of the wind tunnel floor. The free stream and entrance velocities were measured using Pitot-static tubes located along the centre of the test section. In both cases, differential pressures were measured with the same type of pressure transducer as used in the hot-wire

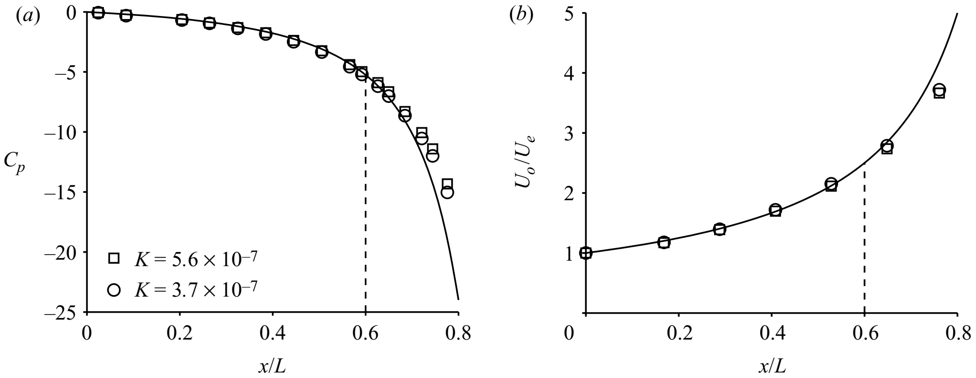

FIGURE 5. Bulk flow properties versus x/L: (*a*) pressure coefficient; (*b*) normalized free stream velocity. The solid lines represent the theoretical behaviour of inviscid sink flow as given by (1.12) and (1.16). The vertical dashed lines represent the expected onset of equilibrium conditions.

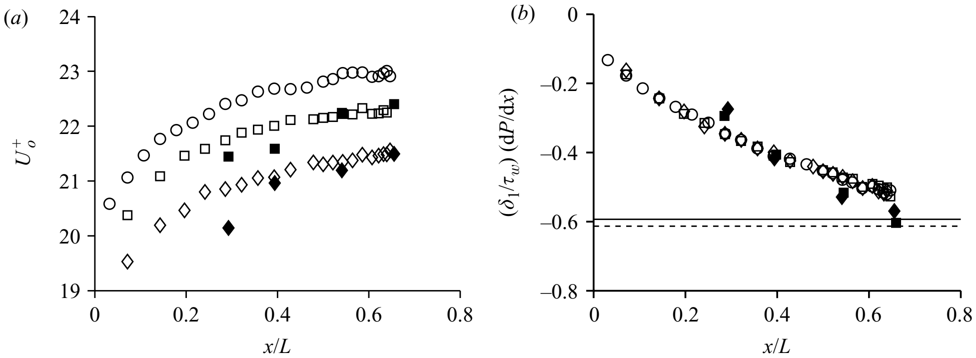

FIGURE 6. Streamwise evolution of (*a*) inner normalized free stream velocity and (*b*) β defined in (1.9). Open symbols from Jones *et al.* (2001): $K(\times 10^7) = 2.7$ ○, 3.6 □, 5.4 ◇. Solid symbols from present data: $K(\times 10^7) = 3.7$ ■, 5.6 ◆. DNS data from Spalart (1986): $K(\times 10^7) = 15$ (solid line), 25 (dashed line).

calibrations. The results are shown in figure 5. The value of $L = 20.3$ m yielded the best curve fit of the theory to the combined U_o and C_p data. The vertical dashed lines denote the approximate onset of equilibrium conditions, according to the study of Jones *et al.* (2001). The present experimental data, for both of the acceleration parameters tested, follow the theoretical curves very well for $x/L \leqslant 0.66$, ensuring that both equilibrium and non-equilibrium behaviours are captured in the present facility. Increasing deviation from the inviscid theory is observed for $x/L > 0.7$ and is attributed to facility end effects. Therefore, only data from $x/L \leqslant 0.66$ are utilized in the present study.

2.5. *Streamwise evolution of bulk flow*

The inner normalized free stream velocity and the parameter β, as defined in (1.9), are shown in figure 6 as functions of streamwise position, compared with the data of Jones *et al.* (2001) for similar acceleration parameters. The data of Jones *et al.* (2001) clearly reveal that U_o^+ approaches a constant value for $x/L > 0.55$. This is consistent with the behaviour of an equilibrium boundary layer as discussed in § 1.1.

For $x/L > 0.5$, the present data agree well with that of Jones *et al.* (2001), while for $x/L < 0.5$, the present U_o^+ values fall below that of Jones *et al.* (2001). Interestingly with regard to the latter observation, when the angled ceiling was not completely sealed to the sidewalls of the wind tunnel, the measured U_o^+ values near the facility entrance ($x/L < 0.5$) were shifted upwards and matched more closely with those of Jones *et al.* (2001). Note Clauser (1954) describes how an improperly sealed ceiling may induce flow leakage out of the facility, thereby leading to an artificial thinning of the boundary layer (developing along the floor of the facility) in an adverse pressure gradient. This effect has been shown to cause an increase in the observed skin friction while approaching separation, contrary to the behaviour predicted by the integral momentum equation. By analogy, for the case of an FPG, leaks in the ceiling may induce an artificial thickening of the boundary layer, which would tend to decrease the measured friction velocity and, hence, increase U_o^+.

In (1.9), the condition that $\beta =$ constant (i.e. independent of x) in the equilibrium regime was shown to follow directly from the assumption of a self-preserving form of the mean momentum balance. Figure 6(*b*) compares the β parameter from the present experiments to that of Jones *et al.* (2001) and Spalart (1986). Note the DNS data of Spalart (1986) are shown as horizontal lines because these data correspond to equilibrium flow only and, thus, are independent of x/L. The trend of the present data agrees with that in Jones *et al.* (2001), i.e. β decreases as $x/L \to 1$, although the slope of the present data is slightly steeper. The data of Jones *et al.* (2001) suggest that the equilibrium value of β (for $x/L \geqslant 0.6$) is -0.51, independent of Reynolds number at least over the range $1000 < Re_\tau < 2000$; however, the equilibrium DNS data of Spalart (1986) indicate $\beta = -0.6$ at $Re_\tau \leqslant 440$. The present equilibrium data, at similar Re_τ compared to Jones *et al.* (2001), agree more closely with the β value from the DNS. According to the analysis in § 1.1, one expects that for a given flow field (specified by $\mathrm{d}P/\mathrm{d}x$), under equilibrium conditions (i.e. when the self-preserving form of the mean momentum balance is valid) β should be independent of both x and Re_τ. The slight discrepancy in this regard between the present experimental study and that of Jones *et al.* (2001) remains to be understood.

3. Mathematical formulation of theory

The mean momentum equation for a two-dimensional steady (in the mean) TBL (Pope 2000, p. 113) is

$$\underbrace{\nu\frac{\partial^2 U}{\partial y^2}}_{F_v} - \underbrace{\frac{\partial\langle uv\rangle}{\partial y}}_{F_t} - \underbrace{\left[U\frac{\partial U}{\partial x} + V\frac{\partial U}{\partial y}\right]}_{F_a} + \underbrace{U_0\frac{\partial U_0}{\partial x}}_{F_p} = 0, \tag{3.1}$$

where U and V are the mean velocity components in the streamwise (x) and vertical (y) directions, respectively, and $\langle uv\rangle$ is the average Reynolds shear stress. From left to right, the terms in (3.1) represent the viscous stress gradient or viscous diffusion (F_v), turbulent or Reynolds shear stress gradient (F_t), total mean advection (F_a) and pressure gradient (F_p). In canonical turbulent wall-bounded flows, such as the fully developed channel and the zero pressure gradient (ZPG) boundary layer, only three terms exist in the mean momentum equation. Specifically, for fully developed channel flow, the balance occurs between F_v, F_t and F_p, whereas in the ZPG case, the balance occurs between F_v, F_t and F_a. Understanding how the combination of F_a and F_p (in balance with F_v and F_t) affects the mean dynamics and scaling properties of the

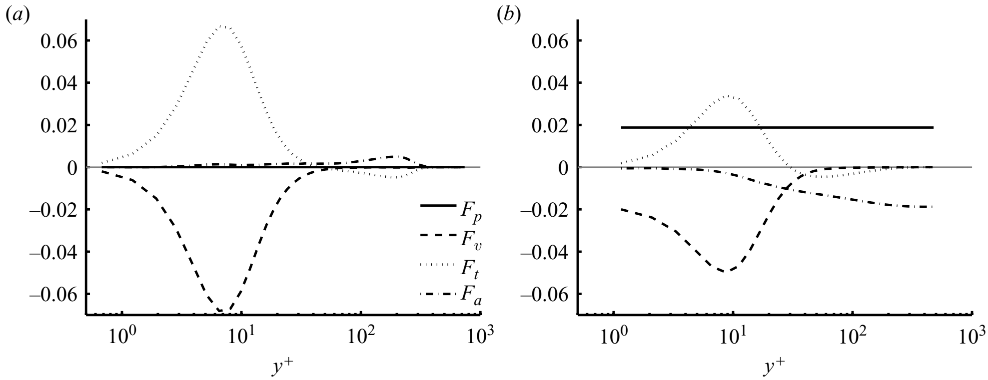

FIGURE 7. Comparison of the magnitudes of the terms in the inner normalized mean momentum balance from DNS data: (*a*) ZPG at $Re_\tau = 300$ and (*b*) FPG at $Re_\tau = 285$, $K = 25 \times 10^{-7}$.

TBL lies at the crux of the present study. Note, the term $\partial/\partial x[\langle u^2\rangle - \langle v^2\rangle]$, which represents the gradient of the Reynolds normal stresses, only becomes non-negligible in flows approaching separation (Castillo & Wang 2004) and is therefore neglected in the present study.

The magnitudes of the terms in the inner normalized mean momentum balance are compared in figure 7, using DNS data from both a ZPG TBL (Spalart 1988) and an equilibrium FPG TBL (Spalart 1986) at similar Re_τ. Available DNS data for other values of Re_τ and K resemble the ones shown in figure 7. The mean momentum balances of the ZPG and FPG TBLs exhibit both similarities and differences, which cannot be attributed to Reynolds number effects. Within the inner region of the boundary layer ($y^+ < 30$), the viscous stress gradient (F_v) and Reynolds stress gradient (F_t) appear to be in approximate balance in both TBLs. The absolute magnitude of the peaks in F_v and F_t, however, are larger in the ZPG case. Furthermore, in the FPG case, the zero crossing of F_t (which corresponds to the peak in the Reynolds stress profile) occurs at a lower y^+, compared to the ZPG TBL. In the outer region ($y/\delta > 0.15$), the Reynolds stress gradient appears to balance the mean advection in the ZPG case, while in the FPG case, the mean advection appears to balance the pressure gradient. In both TBLs, F_v appears to approach zero at rates similar to $y^+ \rightarrow \delta^+$, whereas in the FPG case, F_t approaches zero much more gradually than in the ZPG case. Note also that the mean advection has opposite signs in the two cases.

3.1. *Modelling mean advection*

Figure 7(*b*) shows that the mean advection (F_a) approximately balances the pressure gradient (F_p) in the outer region of the FPG TBL. At the edge of the boundary layer, the mean advection within the boundary layer must, of course, match that of the free stream (i.e. $F_a = F_p$ at $y = \delta$). In addition, F_a must vanish at the wall ($y^+ = 0$), since $U = V = 0$ there, as verified in figure 7(*b*). These observations suggest that the mean advection inside the TBL may be represented as a fraction, $\alpha(x, y)$, of the advection of the potential flow outside the TBL. The proportionality parameter α necessarily depends on both x and y. This leads to the following model of mean advection,

$$\left[U\frac{\partial U}{\partial x} + V\frac{\partial U}{\partial y}\right] = \alpha(x, y)\, U_0\frac{\partial U_0}{\partial x}, \tag{3.2}$$

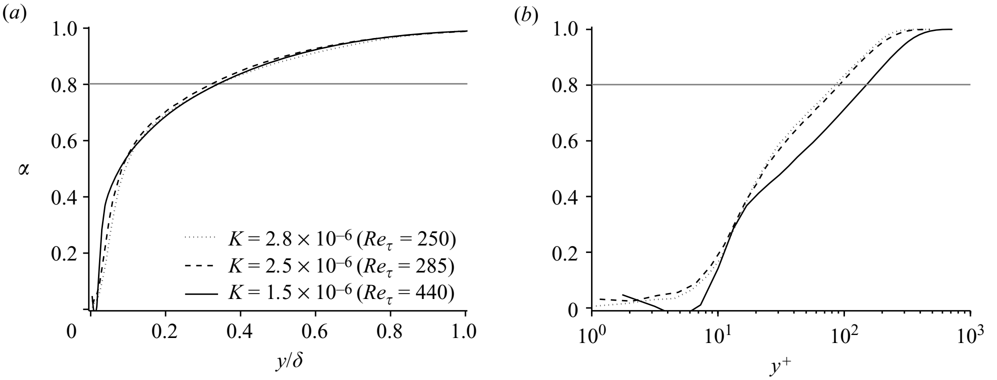

FIGURE 8. Plots of α as functions of distance from the wall, using DNS data: (a) outer normalization; (b) inner normalization. The horizontal grey line represents $\overline{\alpha}$, which remains nearly constant for the three K cases.

where $0 \leqslant \alpha(x, y) \leqslant 1$ to satisfy the boundary conditions. In this view, the potential flow pressure gradient just outside the boundary layer induces advection inside the boundary layer, while the viscous force, due to the presence of the wall, exerts a retarding influence on advection. Therefore, α is predicted to increase monotonically from 0 to 1, as y increases from the wall to the outer edge of the TBL.

Figure 8 illustrates the distinctive properties of α as a function of y^+ and y/δ from the equilibrium FPG data of Spalart (1986). The DNS data are consistent with the above-noted expectations: (i) $\alpha = 0$ at $y = 0$; (ii) $\alpha = 1$ at $y = \delta(x)$; (iii) α increases monotonically with y^+. Note α values for $y^+ < 10$ at the lowest K shown are not accurate because of the propagation of uncertainties in the finite difference scheme used to calculate spatial gradients from the DNS data. Also shown in figure 8 is $\overline{\alpha}$, defined as the average of α over the boundary layer thickness:

$$\bar{\alpha} = \delta^{-1} \int_0^{\delta} \alpha(x, s)\,\mathrm{d}s. \tag{3.3}$$

Within the Re_τ range of the available DNS, only a very weak dependence of $\overline{\alpha}$ on Re_τ exists, with $\overline{\alpha} = 0.812$ at $Re_\tau = 440$. Figure 9 displays $\overline{\alpha}$ as a function of Re_τ from the combined DNS and present experimental data, under equilibrium conditions only (i.e. $x/L > 0.6$ for the experiments). Although it appears that $\overline{\alpha}$ increases nearly linearly with Re_τ, at least over the present Re_τ range, it is intuitive, however, that $\overline{\alpha} \rightarrow 1$ in an asymptotic fashion, as $Re_\tau \rightarrow \infty$. This has implications with respect to the expected change in the α profiles (when plotted versus y/δ) as Re_τ increases and will be revisited in § 5.2.

The proportionality parameter $\alpha(x, y)$ is one of the two principal links that establish the connection between the theoretical study of mean profiles in the FPG TBL with those of the ZPG TBL (or fully developed channel flow). The other principal link will be introduced in § 4.4. At this point, an explicit functional form of $\alpha(x, y)$ is not known theoretically. However, three reasons for why this bears little consequence in the main contribution of the present study are given. First of all, introduction of α allows a reduction in the total number of terms in the force balance, which is significant to making connections between the FPG TBL and canonical wall-bounded flows. Secondly, over the Re_τ range available, α appears to be independent of Reynolds number for $y/\delta > 0.15$, at least, within the uncertainty of the data. (Supporting

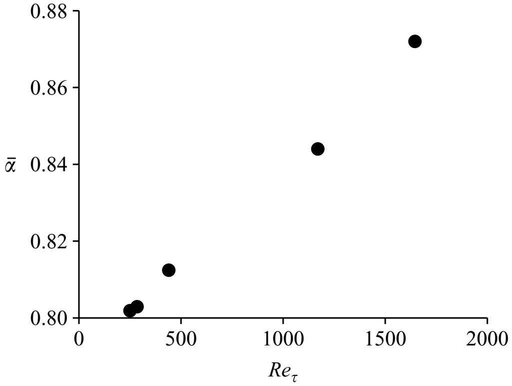

FIGURE 9. Average α versus Re_τ for the FPG equilibrium case only. Data are combined DNS and present experiment data (for $x/L > 0.6$).

experimental data are shown in § 5.2, and important ramifications are discussed in § 5.3.) Thirdly, the known properties of $\alpha(x, y)$, as stated in the previous paragraph, will suffice to provide the order of magnitude results with which the present theory is concerned.

3.2. *Introduction of small parameter* ϵ

Combining (3.1) and (3.2) yields

$$\nu \frac{\partial^2 U}{\partial y^2} - \frac{\partial \langle uv \rangle}{\partial y} + [1 - \alpha(x, y)]\, U_0 \frac{\partial U_0}{\partial x} = 0. \tag{3.4}$$

The inner normalized form of (3.4) can be written as

$$\frac{\partial^2 U^+}{\partial y^{+2}} - \frac{\partial \langle uv \rangle^+}{\partial y^+} + \epsilon^2(x^+)\, b(x^+, y^+, \epsilon) = 0, \tag{3.5}$$

where

$$b(x^+, y^+, \epsilon) = \frac{1 - \alpha(x^+, y^+, \epsilon)}{1 - \overline{\alpha}(x^+, \epsilon)}, \tag{3.6}$$

and ϵ is defined such that

$$\epsilon^2(x^+) = [1 - \overline{\alpha}(x^+, \epsilon)] K(x^+)\, U_0^{+3}(x^+). \tag{3.7}$$

Note for the specific case of a sink-flow TBL, K remains independent of x^+. The relation in (3.7) defines $\epsilon^2(x^+)$ implicitly (explicitly if α is independent of ϵ). It is assumed that ϵ is small. For example in the sink-flow study of Spalart (1986), $1.1 \times 10^{-2} < \epsilon^2 < 2 \times 10^{-2}$ over a Reynolds number range of $250 \leqslant Re_\tau \leqslant 440$. The boundary conditions associated with (3.5) are $U^+ = \langle uv \rangle^+ = 0$ and $\partial U^+/\partial y^+ = 1$ at the wall ($y^+ = 0$) and $\partial U^+/\partial y^+ = \langle uv \rangle^+ = 0$ at the upper edge of the boundary layer ($y^+ = \delta^+$). By integrating (3.5) with respect to y^+ from 0 to δ^+, one obtains a prediction for the inner normalized boundary layer thickness in terms of ϵ:

$$\delta^+(x^+) = \epsilon^{-2}(x^+). \tag{3.8}$$

Thus, the smallness of ϵ^2 may be related directly to the largeness of Re_τ (or, equivalently, δ^+). Note for equilibrium sink-flow TBLs, there is a one-to-one correspondence of Re_τ and K with $Re_\tau \propto K^{-1}$ (Jones *et al.* 2001).

3.3. *The equilibrium state and the analogy with channel flow*

A summary of the main features of the analogy between channel flow and the FPG TBL is given here. First of all, the basic inner normalized differential equation (3.5) has the same appearance as the one for channel flow, except in the channel, $b(x^+, y^+, \epsilon) = 1$. In both flows, the extension of the domain is between $0 \leqslant y^+ \leqslant \delta^+$, where δ^+ is related to ϵ in both flows by (3.8). Furthermore, the boundary conditions are identical at $y^+ = 0$, $U^+ = 0$ and $\partial U^+/\partial y^+ = 1$, while at $y^+ = \delta^+$, $\partial U^+/\partial y^+ = \langle uv \rangle^+ = 0$ and $U^+(x^+, \delta^+) = U_o^+(x^+)$. The formal similarity between the two problems enables techniques and concepts from the study of channel flow (Fife *et al.* 2005*a*, *b*; Wei *et al.* 2005*a*) to be used in the present context of the FPG TBLs as well. In particular, a multi-scale analysis of the inner and outer regions, based on the existence of the small parameter $\epsilon(x^+)$ in the governing equation, is pursued in §§ 4.1 and 4.2 in a manner very similar to channel flow. In addition, a continuum of local natural scales, called scaling patches, is found in § 4.4, using similar methods as in channel flow.

Another similarity between channel flow and the FPG TBL pertains to the behaviour observed in the equilibrium state. One criterion for equilibrium is that U_o^+ remain independent of x^+ (see (1.5)). Therefore, $\partial U_0^+/\partial x^+ \rightarrow 0$ as the flow approaches equilibrium, analogous to the situation in channel flow. This results in an interesting ramification with regard to entrainment (in the mean sense) as the flow approaches equilibrium in the FPG boundary layer, as seen from (3.2), which may be rewritten in inner normalized form as

$$\alpha(x^+, y^+) = \left[U_0^+ \frac{\partial U_0^+}{\partial x^+} \right]^{-1} \left[\left(U^+ \frac{\partial U^+}{\partial x^+} \right) + \left(V^+ \frac{\partial U^+}{\partial y^+} \right) \right]. \tag{3.9}$$

As the flow approaches equilibrium, both $\partial U^+/\partial x^+ \rightarrow 0$ and $V^+ \rightarrow 0$ at the same rate as $\partial U_0^+/\partial x^+ \rightarrow 0$ in order to ensure that α remains bound for all x^+ and y^+. This must hold, since $U^+ \neq 0$ and $\partial U^+/\partial y^+ \neq 0$ throughout the boundary layer (except at the boundaries). The criterion of boundedness for α is also enough to establish the independence of α with respect to x^+ in the equilibrium regime. The fact that $V^+(x^+, y^+) = 0$ implies that the mean dynamics suppress entrainment (on average) of potential core momentum into the boundary layer when the FPG TBL attains an equilibrium state, which is directly analogous to the situation in channel and pipe flow. On the basis of this observation and the fact that α approaches unity in the outer region (figure 8), one might hypothesize that non-equilibrium effects (in the mean profiles) would primarily be manifest in the outer region of the boundary layer, because this is the region immediately affected by entrainment. This notion will be revisited later in § 5.

In channel flow, ϵ $[\equiv (\delta^+)^{-1/2}]$ represents a parameter independent of x^+. In fact, all functions remain independent of x^+ in channel flow. Furthermore, δ^+ is a known quantity (δ from the geometry and u_τ from the integral momentum equation based on knowledge of the imposed pressure gradient driving the flow), while the value of U_o^+ is not known explicitly. In the FPG TBL, although neither U_o^+ nor δ^+ is known explicitly, there will be some function F such that

$$U_o^+(x^+) = F(\epsilon^2, x^+), \tag{3.10}$$

where the x^+-dependence has been retained to account for both equilibrium and non-equilibrium conditions. Note that the dependence of U_o^+ on x^+, besides the inherent x^+-dependence of the parameter ϵ, comes about only through the dependence of b with respect to x^+, as seen in (3.6). This x^+-dependence of U_o^+ is now examined.

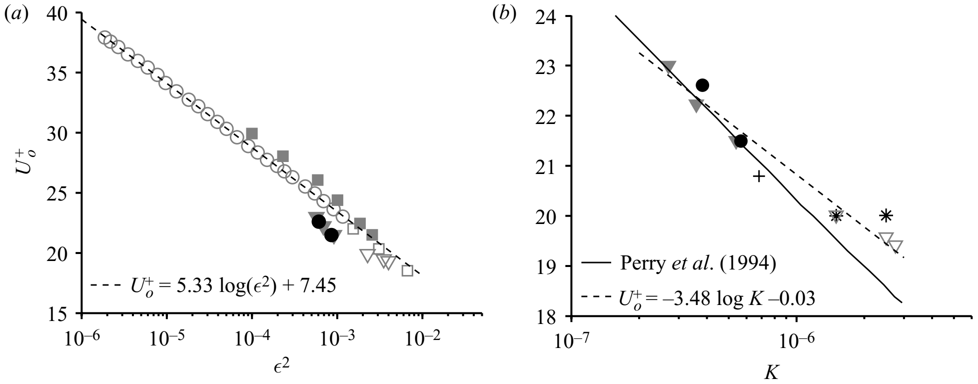

FIGURE 10. Plot of U_0^+ as a function of (a) ϵ^2, comparing pipe flow, ZPG and equilibrium sink flow data and (b) K for equilibrium sink flow only. Superpipe: ○ (McKeon *et al.* 2004); ZPG: □ (Spalart 1988), ■ (Klewicki *et al.* 1990; DeGraaff & Eaton 2000); sink flow: ▽ (Spalart 1986), ▼ (Jones *et al.* 2001), + (Hafez 1991), ∗ (Jones & Launder 1972), • present. The dashed line in (a) represents a curve fit to the Superpipe data only. The dashed line in (b) represents a curve fit to: ▼ ▽ •.

In channel flow where $\beta = 1$, Wei *et al.* (2005a) show that F grows like $C|\ln \epsilon| + D$. In the FPG TBL, it may safely be assumed that F is a decreasing function of ϵ^2, i.e. U_o^+ increases with δ^+, and that $F \to \infty$ as $\epsilon \to 0$. Figure 10(a) compares F for several different flows: Superpipe (McKeon *et al.* 2004); ZPG TBL, experimental (Klewicki *et al.* 1990; DeGraaff & Eaton 2000) and DNS (Spalart 1988); equilibrium FPG TBL, experimental (Jones *et al.* 2001) and DNS (Spalart 1986). At relatively low ϵ^2 (or equivalently high δ^+) in the range $\epsilon^2 < 3 \times 10^{-3}$, a noticeable offset exists between the Superpipe/ZPG data and the equilibrium FPG results; however, the logarithmic trend appears to be the same.

Now recall (3.7) which, along with (3.10), gives $\epsilon^2(x^+) = (1 - \overline{\alpha})K\, [F(\epsilon^2, x^+)]^3$. This can be solved to give $\epsilon^2 = \epsilon^2(K, x^+)$. Putting this dependence back into (3.10), one then obtains a relation between U_0^+, on the one hand, and K and x^+, on the other. Namely for some function S,

$$U_0^+(x^+) = S(K, x^+). \tag{3.11}$$

Figure 10(b) shows S, using previous experimental measurements (Jones & Launder 1972; Hafez 1991; Jones *et al.* 2001) and DNS data (Spalart 1986) from the sink-flow TBL in the equilibrium regime, wherein any x^+-dependence of S has vanished. The theoretical prediction of Perry, Marusic & Li (1994) based on the attached eddy hypothesis is also shown. The data reveal both F and S to be monotone functions, increasing as both ϵ^2 and K decrease. It then follows from (3.7) and (3.11) that $\epsilon^2(x^+) = (1 - \bar{\alpha})K\, [S(K, x^+)]^3$, which shows that the smallness of ϵ^2 is related to the smallness of K. Inserting (3.8) into this expression and considering only equilibrium conditions yields a prediction for the inner normalized boundary layer thickness:

$$\delta^+ = \{(1 - \bar{\alpha})K\, [S(K)]^3\}^{-1}. \tag{3.12}$$

Over the entire Re_τ and K range investigated here, including the present experiments and DNS study of Spalart (1986), a difference of 3 % was observed (on average) between the measured δ^+ and that predicted from (3.12).

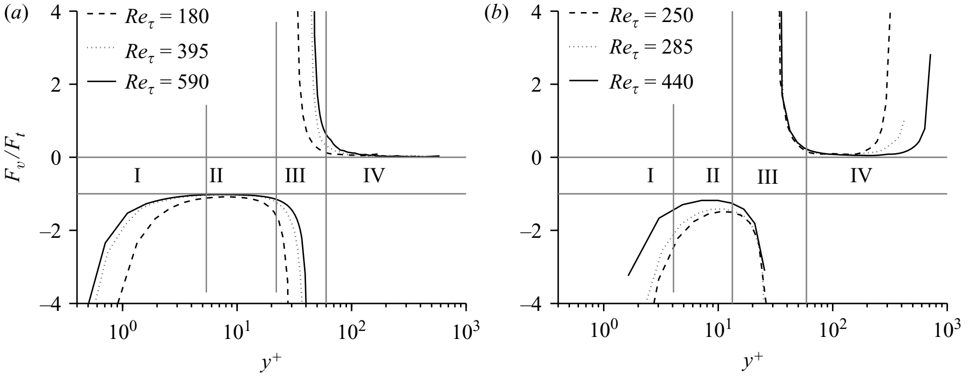

FIGURE 11. Ratio of the viscous diffusion term to the Reynolds stress gradient from DNS data: (*a*) channel (Moser *et al.* 1999) and (*b*) equilibrium FPG TBL (Spalart 1986). Vertical grey lines represent approximate layer boundaries for the intermediate Re_τ case.

4. Layers and scaling domains

The basic differential equation (3.5) with corresponding boundary conditions is formally identical to the one that describes channel flow when $b = 1$. Despite the presence of the factor b in (3.5), most of the same physical layer analysis can be performed, as in the previous work of Wei *et al.* (2005*a*), to reveal the physical layer structure of the FPG TBL in terms of the small parameter $\epsilon(x^+)$. To highlight this, figure 11 shows the ratio of the viscous diffusion term to the Reynolds stress gradient (F_v/F_t), using DNS data for channel flow (Moser, Kim & Mansour 1999) compared to that of the equilibrium FPG TBL (Spalart 1986). Note, Wei *et al.* (2005*a*) observed a marked similarity between the layer structures of channel and the ZPG TBL, although their mathematical analysis focused exclusively on channel flow. In the two cases shown in figure 11, a noticeable layer structure exists, with layers labelled I–IV. Approximate layer boundaries, for the intermediate Re_τ cases only, are marked by vertical grey lines. Reynolds number dependencies of layer boundaries are discussed later in the section.

Each layer is distinguished by the mean dynamics valid in that region of the flow. Since there are only three terms in the force balance governing the mean dynamics, the ratio of two terms is sufficient to describe the behaviour of the system. For example in layer II, the mean dynamics are dominated by a balance between the viscous and turbulent stress gradients, since $F_v/F_t \approx -1$ there. Although qualitative features of the layer structure are preserved in the FPG case, several differences are also revealed. For example the location of layer III in the FPG case does not appear to be dependent on Reynolds number to the extent observed in the channel flow. In addition, a noticeable increase in the ratio of F_v/F_t exists in layer IV in the FPG case. These differences are explored further in the following sections.

4.1. *The inner scaling region*

For the FPG case, inner scaling is valid near the wall for the same reasons as in channel flow. If one sets $T = -\langle uv\rangle^+$, the inner scaled version of (3.5) may be written as

$$\frac{\mathrm{d}^2U^+}{\mathrm{d}y^{+2}} + \frac{\mathrm{d}T}{\mathrm{d}y^+} + \epsilon^2 b(y^+, \epsilon) = 0. \tag{4.1}$$

In the wall region, the last term in (4.1) is $O(\epsilon^2)$ and may be neglected, resulting in an approximate balance between the viscous and Reynolds stress gradients. Figure 11 shows that for very small y^+ (layer I), the viscous stress gradient dominates the Reynolds stress gradient, so that the mean momentum equation may be integrated twice to yield the relation $U^+ \approx y^+$ in layer I. Mean velocity profile data for the sink-flow TBL (Spalart 1986) support this first-order approximation. Including $O(\epsilon^2)$, but still neglecting the Reynolds stress gradient, and integrating leads to the second-order approximation: $U^+ \approx y^+ - (\epsilon^2 y^{+2})/(2-2\overline{\alpha})$. Therefore, in the FPG TBL, mean velocity data very near the wall are expected to fall slightly below the linear profile.

As y^+ increases in layer II, both stress gradients achieve the same order of magnitude, while the pressure gradient/mean advection combination still remains $O(\epsilon^2)$; thus, the linear region (where $U^+ \approx y^+$) ceases to be valid in layer II. It should be emphasized, however, that inner scaling does hold in both layers I and II. Note, in (3.5) and the associated boundary conditions, the variable x^+ appears only as a parameter; i.e. no derivatives with respect to that variable appear explicitly. The approach here will be to treat x^+ as a fixed parameter so that relationships developed for U^+ and $\langle uv\rangle^+$ are assumed valid at every given x^+. For example in layer I, the x^+-dependence of U^+ emerges through the dependence of u_τ on x^+ in such a way that $U^+ \approx y^+$ at every given x^+.

4.2. *The outer scaling region*

Outer scaling will be valid in the region of flow furthest from the wall, adjacent to the potential core (i.e. layer IV). The appropriate outer variable here turns out to be $\eta = \epsilon^2 y^+$ (or, equivalently, $\eta = y/\delta$). From (3.8), it is clear that the edge of the boundary layer resides at $\eta = 1$. The outer scaled version of (3.5) becomes

$$\epsilon^2 \frac{\mathrm{d}^2 U^+}{\mathrm{d}\eta^2} + \frac{\mathrm{d}T}{\mathrm{d}\eta} + b(\eta, \epsilon) = 0, \tag{4.2}$$

where the dependencies on x^+ have been suppressed for simplicity, as noted above. Neglecting ϵ^2 in (4.2) yields an outer approximation $\mathrm{d}T^*/\mathrm{d}\eta = -b(\eta, \epsilon)$. Integrating once yields the decay of the Reynolds stress in the outer region:

$$T(\eta) \approx \int_\eta^1 b(s, \epsilon)\,\mathrm{d}s \equiv T^*(\eta, \epsilon). \tag{4.3}$$

Note $T^*(0, \epsilon) = 1$ and $T^*(1, \epsilon) = 0$. Also, the first two derivatives of T^* vanish at $\eta = 1$, and so T^* is rather flat there. However, T^* is not a good approximation to T in a neighbourhood of $\eta = 0$ (near the wall). As η decreases from 1, the true function $T(\eta)$ rises to a peak value near $T^*(0, \epsilon)$ and then drops again near the wall to satisfy $T(0) = 0$.

Except for the smooth approach to the upper value $T(1) = 0$, due to the presence of α, the T for the FPG case has the same qualitative behaviour as in channel flow (see Wei *et al.* 2005*a*). Figure 12 demonstrates that the prediction in (4.3) compares quite well with the DNS data of Spalart (1986) near $\eta = 1$. Because of the asymptotic nature of the theory, the agreement is expected to improve as $\epsilon \to 0$ (or, equivalently, $Re_\tau \to \infty$). Note, the integral in (4.3) is evaluated using the α profile at $Re_\tau = 440$ (as shown in figure 8). Over the narrow Reynolds number range investigated in the DNS study, the trend appears to be that as $\epsilon \to 0$, T increases to a limiting T^*. An important ramification is that low Reynolds number DNS data may be sufficient to determine the high Re_τ behaviour of T in the outer region of the flow near $\eta = 1$, since the outer flow behaviour of T depends entirely on $\alpha(\eta, \epsilon)$, which appears to

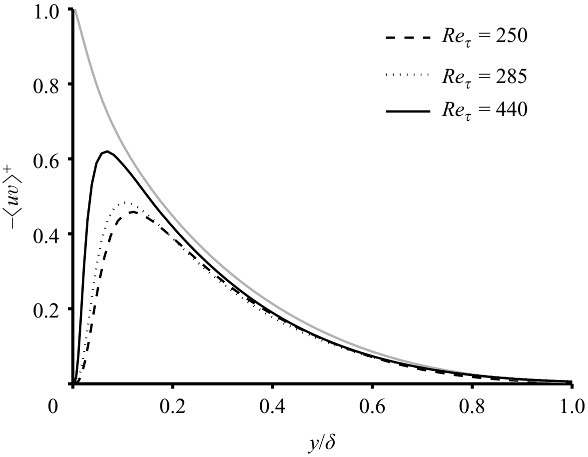

FIGURE 12. Inner normalized Reynolds stress versus the outer scaled wall-normal coordinate, using the sink-flow DNS data of Spalart (1986). The grey line represents the theoretical T^* as given by (4.3).

be relatively independent of Re_τ for $\eta > 0.15$. Experimental results in § 5.3 further substantiate this observation.

4.3. *The mesolayer*

In the mesolayer (associated loosely with layer III in figure 11), it will be shown that the wall-normal coordinate scales with the geometric mean of the inner and outer scales. In order to obtain this result, it is useful to work with a modified Reynolds stress, defined as

$$\tilde{T} \equiv T - T^* - \eta, \tag{4.4}$$

where T^* denotes the outer layer approximation as given by (4.3). Taking the derivative with respect to y^+, using the facts that $\mathrm{d}\eta/\mathrm{d}y^+ = \epsilon^2$ and $\mathrm{d}T^*/\mathrm{d}y^+ = -\epsilon^2 b(\eta, \epsilon)$, gives

$$\frac{\mathrm{d}\tilde{T}}{\mathrm{d}y^+} = \frac{\mathrm{d}T}{\mathrm{d}y^+} + \epsilon^2 b(\eta, \epsilon) - \epsilon^2. \tag{4.5}$$

Substituting this into (4.1) yields

$$\frac{\mathrm{d}^2 U^+}{\mathrm{d}y^{+2}} + \frac{\mathrm{d}\tilde{T}}{\mathrm{d}y^+} + \epsilon^2 = 0. \tag{4.6}$$

In channel flow, the mesolayer occurs at the peak in T (Wei *et al.* 2005*a*). In the present case, however, the mesolayer occurs at the peak in $\tilde{T}$. The difference in the location of these peaks is small, as shown from (4.5). Specifically, when $\mathrm{d}T/\mathrm{d}y^+ = 0$, $\mathrm{d}\tilde{T}/\mathrm{d}y^+ = \epsilon^2(b-1)$, indicating that the peak in $\tilde{T}$ occurs at slightly higher y^+ compared to the peak in T. For example from the DNS data at $Re_\tau = 440$, $b = 2.75$ at the location of the peak in T. Since $b = O(1)$, $\mathrm{d}\tilde{T}/\mathrm{d}y^+ = O(\epsilon^2)$ when $\mathrm{d}T/\mathrm{d}y^+ = 0$, which guarantees that the location of the peak in T is close to the peak in $\tilde{T}$.

As y^+ increases across layer II, $\tilde{T}$ rises to a peak, at which point the middle term in (4.6), $\mathrm{d}\tilde{T}/\mathrm{d}y^+$, vanishes. As $\mathrm{d}\tilde{T}/\mathrm{d}y^+$ approaches 0, a place must exist where $\mathrm{d}\tilde{T}/\mathrm{d}y^+$ equals ϵ^2, i.e. becomes the same order of magnitude as the last term in (4.6). Near that point, which is in a neighbourhood of the peak in $\tilde{T}$, all three terms in (4.6) have the same order of magnitude. It is then appropriate, and possible, to rescale the variables such that all terms in (4.6) are nominally $O(1)$.

Similar to the approach used for channel flow (Wei *et al.* 2005*a*), such a rescaling is accomplished by defining

$$y^+ = y_m^+ + \epsilon^\zeta \hat{y}, \quad U^+ = U_m^+ + \epsilon^\xi \hat{U}, \quad \tilde{T} = \tilde{T}_m + \epsilon^\psi \hat{T}, \tag{4.7}$$

where $\hat{U}$, $\hat{T}$ are $O(1)$ functions of $\hat{y}$ and ϵ; $\tilde{T}_m$, U_m^+ are the values of $\tilde{T}$, U^+ at y_m^+, which define the location of the peak in $\tilde{T}$. Since the theory deals only with orders of magnitude of the scaling factors (ϵ^ξ, ϵ^ζ, ϵ^ψ), there is no loss of generality in taking the coefficients of these powers of ϵ to be unity. In addition, the linear parts of U^+ and $\tilde{T}$ are irrelevant to this scaling exercise because they contribute nothing to the two derivatives in (4.6).

Substituting these into (4.6) and requiring all terms to have equal orders of magnitude leads to $\zeta = (\xi - 2)/2$ and $\psi = (\xi + 2)/2$, where ξ is taken to be arbitrary. Thus,

$$\mathrm{d}\hat{y} = \epsilon^{-(\xi-2)/2}\,\mathrm{d}y^+, \quad \mathrm{d}\hat{U} = \epsilon^{-\xi}\mathrm{d}U^+, \quad \mathrm{d}\hat{T} = \epsilon^{-(\xi+2)/2}\mathrm{d}T. \tag{4.8}$$

This leads to the properly scaled mean momentum balance near the peak in the Reynolds stress profile

$$\frac{\mathrm{d}^2\hat{U}^+}{\mathrm{d}\hat{y}^2} + \frac{\mathrm{d}\hat{T}}{\mathrm{d}\hat{y}} + 1 = 0. \tag{4.9}$$

The rescaled functions satisfy $\hat{T}(0) = \mathrm{d}\hat{T}/\mathrm{d}\hat{y}(0) = 0$, $\mathrm{d}^2\hat{U}^+/\mathrm{d}\hat{y}^2(0) = -1$. The region of the boundary layer where this scaling holds is called the mesolayer, meaning that $\hat{U}$ and $\hat{T}$ are regular functions of $\hat{y}$ there. The mesolayer does not coincide exactly with physical layer III because of the difference between T and $\tilde{T}$, as described earlier.

An analogous scaling will be performed in § 4.4 for a whole continuum of patches. It will be argued, based on other theories and empirical evidence, that the unknown parameter ξ is probably either 0 or negative and small. In the following, it is assumed that $\xi = 0$, in which case the length scale in the mesolayer becomes $\mathrm{d}\hat{y} = \epsilon\,\mathrm{d}y^+$. Thus, the scaling in the mesolayer is intermediate between the inner scaling $\mathrm{d}y^+$ and the outer scaling $\mathrm{d}\eta$ and specifically represents the geometric mean between these two scales; i.e. $\hat{y} = y/\sqrt{\delta\,(\nu/u_\tau)}$, where δ denotes the integral (outer) length, and (ν/u_τ) denotes the viscous (inner) length. Appendix A shows theoretically that the location of the mesolayer (y_m^+), and thus the peak in the *modified* Reynolds stress profile, is at $y^+ = O(\epsilon^{-1})$. This is also the same order of magnitude of the width of the mesolayer. Importantly, this predicts that the location of the peak in $\tilde{T}$ scales like $\sqrt{\delta^+}$ as $\delta^+ \to \infty$; i.e. $y_m^+/\sqrt{\delta^+}$ remains constant as $Re_\tau \to \infty$. Experimental results presented in § 5.3 support this theoretical prediction.

4.4. *The hierarchy of scales*

In this section, a continuum or hierarchy of scales is shown to exist in the FPG TBL, analogous to that in the channel flow as originally formulated by Fife *et al.* (2005*a,b*). Furthermore, it is shown that this family of scaling patches covers the entire boundary layer. The inner scale, mesoscale and outer scale, described above, are associated with particular scaling domains (patches) embedded within, or at one of the ends of, the hierarchy. For example rather than treating it as an a priori known feature of the flow, the outer scaling region is considered the culminating scaling patch at the edge of the hierarchy. A scaling patch is defined here as a region in the flow field, specified by an interval of distances from the wall, wherein a 'natural' scaling exists that succeeds in removing Reynolds number trends in the normalized variables. In contrast, 'physical layers' are regions in the flow characterized by the types of forces in balance there. Each scaling patch has distinct scaling coefficients which convey, for example characteristic lengths and Reynolds stress increments at that location. The locations of the patches and the characteristic length scale in each patch are found in Appendices A and B, respectively.

To obtain the scale hierarchy, a family of adjusted Reynolds stresses is defined as

$$T_\beta(y^+) \equiv T(y^+) - T^*(\epsilon^2 y^+, \epsilon) - \beta y^+, \tag{4.10}$$

where $T^*(\epsilon^2 y^+, \epsilon)$ is given by (4.3). Recall that $\eta = \epsilon^2 y^+$. The subscript β (not to be confused with the equilibrium parameter identified by Bradshaw in § 1.1) parameterizes the family and, as will be shown, also identifies the characteristic lengths in the corresponding scaling patches. The locations of the patches are where $T_\beta(y^+)$ attain their maxima. Inserting (4.10) into (4.1), while noting that $\mathrm{d}T^*/\mathrm{d}\eta = -b(\eta, \epsilon)$, yields

$$\frac{\mathrm{d}^2 U^+}{\mathrm{d}y^{+2}} + \frac{\mathrm{d}T_\beta}{\mathrm{d}y^+} + \beta = 0. \tag{4.11}$$

Note (4.11) and (4.6) are identical for the case of $\epsilon = \beta^{1/2}$. As in the approach used in the previous section, the variables in (4.11) will now be rescaled in order to remove the explicit dependence of β in the differential equation. For each β in a range of values that depends on δ^+, the function $T_\beta(y^+)$ has a strict local maximum at some point $y^+ = y_m^+(\beta)$, also dependent on δ^+. As in the channel (Fife *et al.* 2005*a*,*b*), each potential scaling patch, denoted as L_β, will be centred around the peak position $y_m^+(\beta)$ of the associated adjusted Reynolds stress T_β. From the previous analysis in the mesolayer, the intrinsic scaling for the β patch is obtained from (4.8):

$$\mathrm{d}y^+ = \beta^{(\xi-2)/4}\mathrm{d}\hat{y}, \quad \mathrm{d}T_\beta = \beta^{(\xi+2)/4}\mathrm{d}\hat{T}, \quad T_\beta = T_{\beta_m} + \beta^{(\xi+2)/4}\hat{T}. \tag{4.12}$$

For the case of $\xi = 0$, analogous to (4.8),

$$\mathrm{d}y^+ = \beta^{-1/2}\mathrm{d}\hat{y}, \quad \mathrm{d}T_\beta = \beta^{1/2}\mathrm{d}\hat{T}, \quad T_\beta = T_{\beta_m} + \beta^{1/2}\hat{T}, \tag{4.13}$$

where $T_{\beta_m} = \max(T_\beta)$. In all cases, the scaling (4.12) leads to a parameter-free differential equation:

$$\frac{\mathrm{d}^2 U^+}{\mathrm{d}\hat{y}^2} + \frac{\mathrm{d}\hat{T}}{\mathrm{d}\hat{y}} + 1 = 0. \tag{4.14}$$

The two derivatives shown in (4.14) take on known values at $\hat{y} = y_m^+$, namely −1 and 0, respectively.

Although the patches are at different locations, the dynamics in each patch satisfy (4.14), the same differential equation, when the variables in the patch are scaled as given in (4.13). This suggests that the scaled profiles, in the various patches, bear similarity to one another. Firstly, all the profile functions will have derivatives of order $O(1)$, as described earlier. Secondly, it is suggested that these derivatives themselves are almost independent of β. It turns out that the range of the parameter β for which this construction is allowed spans the interval (ϵ^4, β_0), where $\beta_0 = O(1)$, and the locations of the patches, measured in the inner coordinate, span an interval from the inner scaling region to the outer one. The length of this interval is $O(\epsilon^{-2})$, which is large when ϵ is small.

Each potential patch (identified herein as L_β) is centred around the peak position $y_m^+(\beta)$ of the associated adjusted Reynolds stress T_β. The curvature of $\hat{T}$ at its peak is, of course, given by the second derivative of $\hat{T}$ evaluated at the local maximum of

T_β, namely at $\hat{y}=0$,

$$A(\beta) \equiv \frac{\mathrm{d}^2\hat{T}}{\mathrm{d}\hat{y}^2}(0). \tag{4.15}$$

The order of magnitude of this quantity remains $O(1)$ independent of β. In locations far away from the endpoints of the range of the continuum of scaling patches, A should be almost constant. The hypothesis is that since the differential equation is parameter-independent, any variation in A due to changes in β will be caused only by influence from neighbouring patches, hence ultimately from locations where the boundary would introduce other, external influences in such a way as to disrupt the similarity. Most likely, this would happen near the extrema of the continuum (i.e. in the outer and inner regions of the boundary layer). That leaves interior regions as candidates for places where A is nearly constant. It will be shown below that those are the regions where the mean velocity profile exhibits logarithmic behaviour. The extent (in inner units) of these regions will grow as ϵ becomes smaller (i.e. Re_τ increases). All these considerations were explored in the contexts of turbulent channel and Couette flows (Fife *et al.* 2005*a*, *b*; Wei *et al.* 2005*a*), and they are now seen to be valid in the FPG TBL case as well. The fact that the scale hierarchy is preserved even in the boundary layer context with the addition of an FPG also suggests an important similarity in the underlying physical structure of the FPG TBL compared to canonical wall-bounded flows.

4.5. *Conditions for logarithmic mean velocity profile*

One of the hallmarks of the study of turbulent channel flow has been the recognition that a portion of the mean velocity profile exhibits a logarithmic behaviour (Pope 2000). The analysis here, drawing upon the earlier work of Fife *et al.* (2005*a*, *b*) for the channel flow, focuses on the conditions under which such a logarithmic velocity profile will be realized in the FPG TBL. The simplest analysis, in this regard, occurs when $A(\beta)$ is constant. Straightforward calculations, as explained in Appendix A, then show that $U^+ = C_1 \ln(y^+ + C_2)$, where C_1, C_2 are constants. The present data as well as previous DNS and experimental studies support this calculation, as shown in § 5 as well as in figure 4 from Spalart (1986) and figure 5 from Jones *et al.* (2001). Conversely, if A is not constant, then the profile will not be logarithmic. When A is only approximately constant for a given range in β, the more likely circumstance, then U^+ will be approximately logarithmic for the corresponding range of y^+.

5. Experimental results

Throughout this section, results are presented comparing non-equilibrium and equilibrium flow. Typically, two plots are displayed side-by-side that distinguish between (*a*) non-equilibrium effects at a fixed acceleration parameter, $K = 3.7 \times 10^{-7}$, and (*b*) Reynolds number effects observed in the equilibrium regime. In the latter case, the present experimental data are compared with the DNS data of Spalart (1986). In the former case, the present experimental data are compared over a range of x/L (at a fixed K). Since non-equilibrium effects at $K = 5.6 \times 10^{-7}$ were identical to those observed at $K = 3.7 \times 10^{-7}$, only non-equilibrium data at the lowest K are shown. Note for a sink-flow TBL in equilibrium, the Reynolds number is a function of the acceleration parameter only (see (3.12) as well as figure 14 from Jones *et al.* 2001), whereas in the non-equilibrium case, the Reynolds number is a function of both K and x/L.

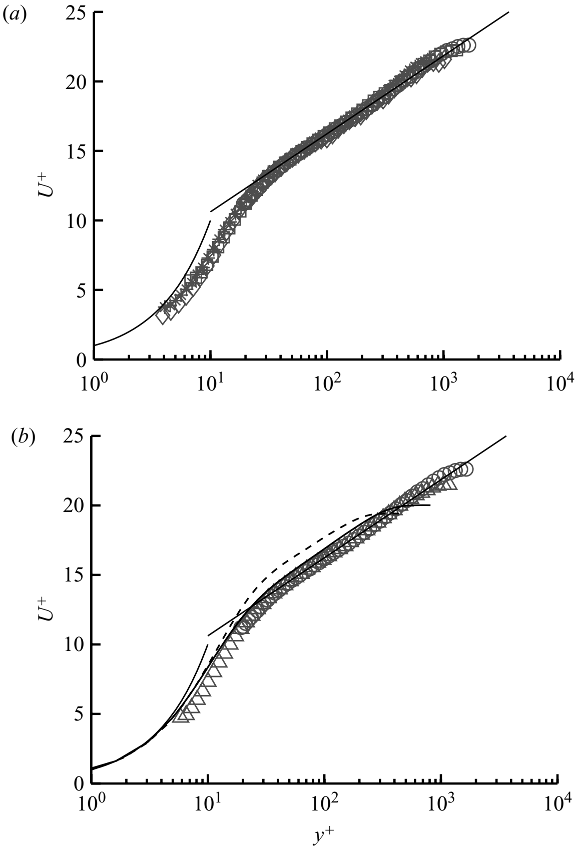

FIGURE 13. Inner normalized mean streamwise velocity profiles showing (*a*) non-equilibrium effects at $K = 3.7 \times 10^{-7}$ and (*b*) Reynolds number effects in the equilibrium case. Symbols and thick lines are identified in table 1. The two thin black lines represent the linear profile ($U^+ = y^+$, for $y^+ < 10$) and logarithmic profile ($U^+ = 2.5 \ln y^+ + 5.0$, for $y^+ > 10$).

5.1. *Mean and r.m.s. velocity profiles*

The inner normalized mean profiles are shown in figure 13 in the format described above. All of the experimental data, regardless of Re_τ or x/L, exhibit a well-defined logarithmic region. Both DNS data sets ($Re_\tau = 285$, 440) exhibit smaller logarithmic regions that are slightly shifted upwards compared to the experimental data. This demonstrates the fact that as Re_τ decreases (or K increases), the mean profile tends towards that expected for a laminar boundary layer. Narasimha & Sreenivasan (1979) suggest that when the acceleration parameter increases to a value near $K = 2.5 \times 10^{-6}$, the TBL approaches a relaminarized state; the data of Jones & Launder (1972) support this. Note that although the present experimental data are forced to follow the log law with constants as specified in figure 13 (due to the nature of the Clauser method used to obtain u_τ), the behaviour of the present U^+ profiles agrees very well with those of Jones *et al.* (2001), who found that the Clauser method (using the same constants) yields an accurate measure of u_τ in the FPG TBL, at least over the range of K investigated here. The present U^+ data also support previous observations that the wake component becomes negligible as the sink-flow TBL approaches equilibrium (Coles 1957; Jones *et al.* 2001). In addition, the fact that the present U^+ data for

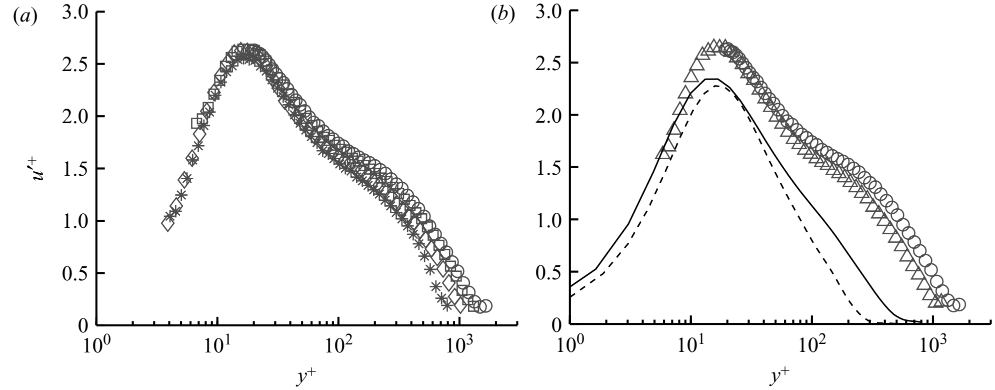

FIGURE 14. Inner normalized streamwise r.m.s. velocity profiles showing (*a*) non-equilibrium effects at $K = 3.7 \times 10^{-7}$ and (*b*) Reynolds number effects in the equilibrium case. Symbols and lines are as in table 1.

$y^+ < 8$ fall slightly below the line representing a linear velocity profile ($U^+ = y^+$) is consistent with the effect of a second-order correction due to the pressure gradient term in the mean momentum balance, as discussed in § 4.1.

Figure 14 depicts the inner normalized r.m.s. velocity profiles for both the equilibrium and non-equilibrium regimes. Near the wall ($y^+ < 10$), all of the profiles, excluding the lowest Re_τ from the DNS data, appear to be independent of Re_τ, x/L and K. In figure 14(*a*), the peak value of u'^+ (near $y^+ = 18$) increases slightly with x/L, as expected, since Re_τ also increases accordingly with x/L. In the outer region beyond the peak, the increase in u'^+ with Re_τ becomes more pronounced, and a shoulder begins to emerge in the profile around $y^+ = 200$. The location of the peak in u'^+ does not appear to depend on Re_τ (or x/L) over the parameter range investigated here. These trends are also observed in figure 14(*b*) for the equilibrium data. The difference in Reynolds number between the DNS and experimental data is almost an order of magnitude. Thus, it is not surprising that the peak u'^+ from the DNS data lies noticeably below that of the experimental data. In addition, no apparent shoulder exists in the DNS profiles, which further indicates possible low Re_τ effects in the DNS data, similar to those discussed by Murlis, Tsai & Bradshaw (1982) for the ZPG TBL and also noticeable in the log region of the U^+ profiles shown in figure 13.

The corresponding outer normalized r.m.s. velocity profiles are shown in figure 15, using semi-log coordinates along the abscissa. The equilibrium profiles (from the experimental data) in figure 15(*b*) appear to be independent of Re_τ for $y/\delta > 0.1$. Due to supposed low Reynolds number effects, the equilibrium DNS data do not exhibit the same similarity in the outer region until further towards the edge of the boundary layer, i.e. $y/\delta > 0.3$. Figure 15(*a*) highlights the effect of x/L on u'^+. For reference, the solid black line in figure 15(*a*) represents the equilibrium data at $K = 5.6 \times 10^{-7}$ (i.e. the same data as that marked by triangles in figure 15*b*). The value of the Reynolds number associated with this line is 1170, which falls between that of the diamonds ($Re_\tau = 1018$, $x/L = 0.39$) and the squares ($Re_\tau = 1307$, $x/L = 0.54$). Note, the two data sets marked by the diamonds and squares are considered to be in non-equilibrium, since $x/L < 0.6$. In the inner region ($y/\delta < 0.1$), the equilibrium data (solid black line) lies directly between the two non-equilibrium data sets (diamonds and squares), suggesting that in the inner region the observed trends in figure 15(*a*) are primarily due to Reynolds number effects and not due to the equilibrium state of

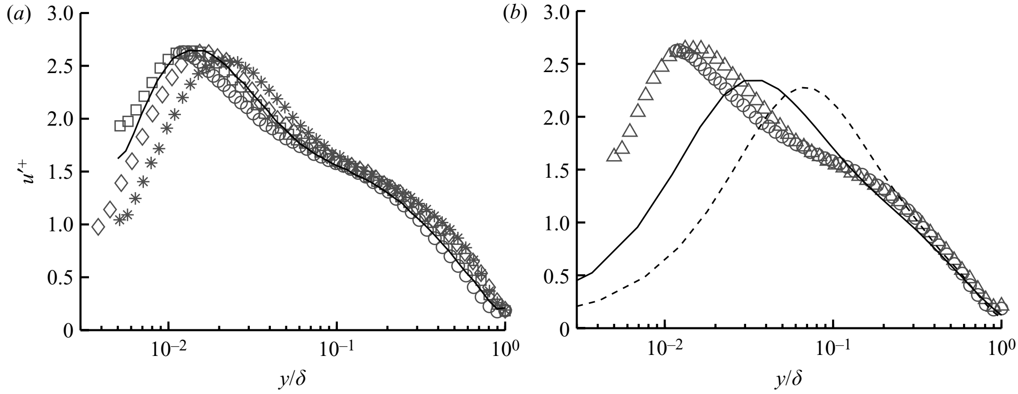

FIGURE 15. Outer normalized streamwise r.m.s. velocity profiles showing (*a*) non-equilibrium effects at $K = 3.7 \times 10^{-7}$ and (*b*) Reynolds number effects in the equilibrium case. Symbols and lines are as in table 1, except that the solid black line in (*a*) and the triangles in (*b*) represent the same equilibrium data at $K = 5.6 \times 10^{-7}$.

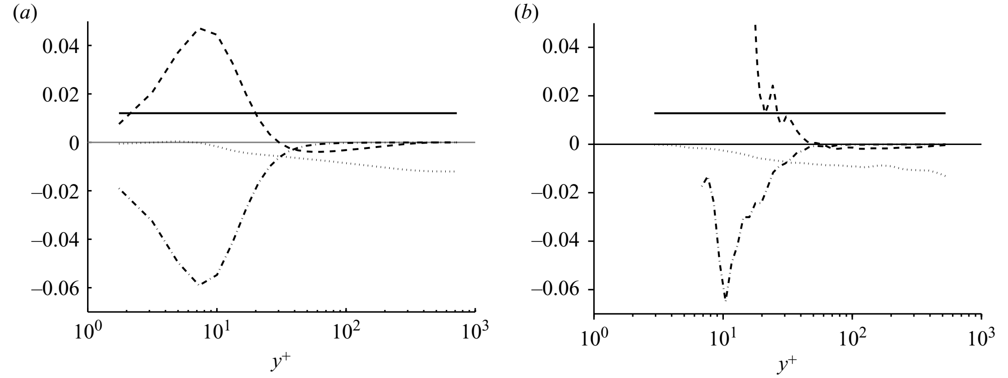

FIGURE 16. Terms in the inner normalized mean momentum balance for an FPG TBL: (*a*) DNS data at $Re_\tau = 440$ and (*b*) present data at $Re_\tau = 540$, $x/L = 0.3$. The terms are identified in (3.1): — F_p, —— F_t, ⋯ F_a, — · — F_v.

the flow (i.e. x/L). In the outer region ($y/\delta > 0.1$), on the other hand, the equilibrium data at $K = 5.6 \times 10^{-7}$ (solid black line) follow the equilibrium data at $K = 3.7 \times 10^{-7}$ (circles), whereas the non-equilibrium data in the outer region have distinctly higher u'^+ values. This suggests that non-equilibrium effects are manifest predominantly in the outer region of the flow. This observation is revisited further in the next two sections.

5.2. *Terms in the mean momentum balance*

The terms in the mean momentum balance are shown in figure 16 for qualitative purposes only, comparing the equilibrium DNS data at $Re_\tau = 440$ with the present non-equilibrium experimental data at a similar Reynolds number, $Re_\tau = 540$, and $x/L = 0.29$. The terms calculated from the experimental data resemble that of the numerical data both in shape and magnitude, although the noise in the experimental data, associated with the finite difference operation for estimating derivatives, is clearly visible. The lack of F_t data for $y^+ < 18$ is due to the physical limitations of positioning the x-array probe in close proximity with the wall. The data in figure 16

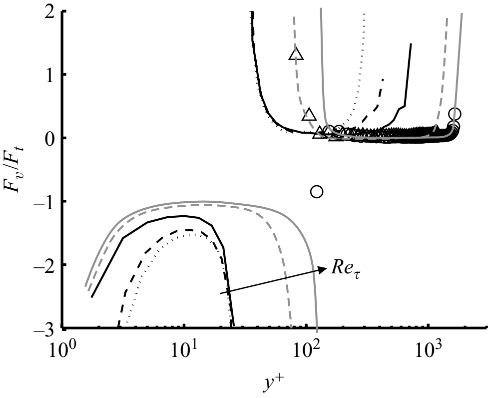

FIGURE 17. Ratio of the viscous stress gradient to the Reynolds stress gradient as a function of y^+ for the DNS and experimental data (equilibrium case only). Symbols are as in table 1, except the grey lines, which represent the *expected* behaviour of the experimental data at – – – $Re_\tau = 1170$ and —— $Re_\tau = 1646$.

show that the viscous and Reynolds stress gradients dominate the flow near the wall until $y^+ \approx 30$, whereafter a clear exchange of balance occurs (across layer III) such that the mean advection (inside the boundary layer) and the pressure gradient become the dominating terms near the outer edge of the boundary layer. Interestingly, this exchange at $y^+ \approx 30$ corresponds to the point in figure 13 at which the inner normalized mean velocity profile begins to be characterized by the log law. The location of this exchange also corresponds with the peak in the Reynolds shear stress profile (i.e. the zero crossing of F_t). Note, as $\epsilon \rightarrow 0$, the magnitude of the inner normalized pressure gradient term F_p moves closer towards zero, but the exchange of balance is preserved.

Based on the observations in figure 16 regarding the balance of terms in the mean momentum equation, it is useful to examine the ratio of the two stress gradient terms. Figure 17 displays this ratio for the equilibrium cases only; the solid and dashed grey curves correspond to the *expected* behaviour of the ratio (based on the theory presented in §4) for the experimental data at $Re_\tau = 1646$ and 1170, respectively. In particular, the theory predicts that as $Re_\tau \rightarrow \infty$, $F_v/F_t \rightarrow -1$ in layer II, where the predominant balance occurs between the viscous and Reynolds stress gradients. Since Reynolds stress measurements are difficult to obtain near the wall, no experimental data exist for F_t in layer II. As the Reynolds stress profile approaches its peak value y^+_{peak}, the Reynolds stress gradient F_t approaches a zero crossing such that $F_v/F_t \rightarrow \infty$ (in layer III). Therefore, the location of the peak in the Reynolds stress profile appears as an asymptote in the plot of F_v/F_t and represents the transition point for the balance exchange. The location of this asymptote appears to shift towards higher y^+ as the Reynolds number increases. This indicates that layer II, where the predominant balance exists between the viscous and Reynolds stress gradients, grows in viscous units as the Reynolds number increases.

The mean advection term, F_a, may be separated into horizontal ($U^+\partial U^+/\partial x^+$) and vertical ($V^+\partial U^+/\partial y^+$) components. Figure 18 shows the magnitude of these two components as a function of x/L for the case of $K = 3.7 \times 10^{-7}$. The dashed lines in figure 18(a) represent the total mean advection. The vertical advection of momentum is, as expected, directed towards the wall. At the edge of the boundary layer, the

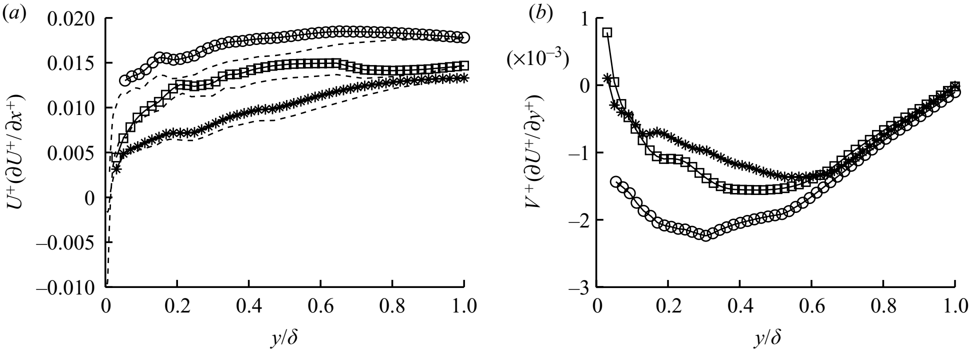

FIGURE 18. Profiles of (a) horizontal advection and (b) vertical advection for the case of $K = 3.7 \times 10^{-7}$. Symbols are as in table 1. The dashed lines indicate the total mean advection (sum of the horizontal and vertical components).

vertical advection goes to zero (regardless of x/L) due to the boundary condition $\partial U^+/\partial y^+ = 0$ at $y/\delta = 1$. Therefore, the vertical advection profiles appear to be independent of x/L near the edge of the boundary layer. As the flow approaches equilibrium, the location of the minimum in the vertical advection component appears to migrate toward the wall (in terms of outer units) from $y/\delta \approx 0.6$ at $x/L = 0.29$ to $y/\delta \approx 0.3$ at $x/L = 0.66$. Furthermore, as the flow approaches equilibrium, the vertical component of the advection increases in absolute magnitude and can be as much as 15 % of the total advection. In addition, as the flow progresses towards equilibrium, the horizontal advection component becomes flatter in the outer region ($y/\delta > 0.1$) and increases in magnitude across the entire boundary layer, due to the fact that Re_τ increases simultaneously with x/L, resulting in an overall increase in U_o^+.

After examining the nature of the separate components of the mean advection, it is useful to examine its behaviour with respect to the advection at the edge of the boundary layer, i.e. with respect to the pressure gradient term F_p. Figure 19 shows this ratio, α, defined in (3.2), as a function of y/δ for both the non-equilibrium and equilibrium regimes. The experimental data are consistent with the theory (§ 3.1) in that $\alpha = 0$ at $y = 0$ and $\alpha = 1$ at $y/\delta = 1$, ensuring $F_a = F_p$ at the edge of the boundary layer, and that α increases monotonically with y/δ. Note that undulations in the α profiles are presumedly due to noise caused by numerical differentiation of the experimental data. Despite the noise, several observations can be made. First, the equilibrium α profiles appear to be independent of Re_τ towards the edge of the boundary layer ($y/\delta > 0.2$). Also for the equilibrium case, the near-wall slope of α increases dramatically with Re_τ, indicating that the increase in α in the near-wall region accounts for the Reynolds number dependence of $\overline{\alpha}$, as shown previously in figure 9. Due to this effect, the region wherein the mean advection approximately balances the pressure gradient (layer IV) expands in outer units with Re_τ, i.e. layer IV appears to extend further towards the wall in terms of y/δ as Re_τ increases.

At this point, a hypothesis regarding the equilibrium sink-flow TBL emerges based entirely on observations of the data. Since layer II (the region where the Reynolds and viscous stress gradients approximately balance) grows in viscous units, while layer IV (the region in which the mean advection and pressure gradient approximately balance) grows in outer units with increasing Re_τ, it may be hypothesized that layer III (where an exchange of balance occurs) must grow like the arithmetic mean between the inner

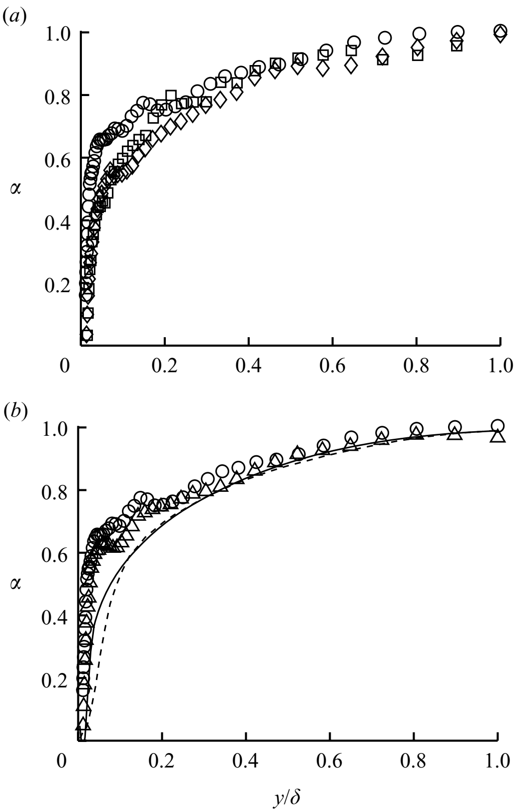

FIGURE 19. Profiles of α showing (a) non-equilibrium effects at $K = 3.7 \times 10^{-7}$ and (b) Reynolds number effects in the equilibrium case. Symbols and lines are as in table 1.

and outer units. This scenario, in fact, is predicted by the present multi-scale theory, as described in § 4.3, and further substantiated by the present Reynolds stress results shown in the next section.

Non-equilibrium effects in the α profiles at a fixed K are displayed in figure 19(a). Recall that the equilibrium data marked by the triangles in figure 19(b) are characterized by $Re_\tau = 1170$, which lies halfway between the Reynolds numbers of the non-equilibrium data in figure 19(a) marked by the diamonds ($Re_\tau = 1018$, $x/L = 0.39$) and the squares ($Re_\tau = 1307$, $x/L = 0.54$). These combined data reveal that $\alpha_{non} < \alpha_{eq}$ for all y/δ, except at the boundaries where the value of α remains fixed. The subscripts represent 'non-equilibrium' and 'equilibrium' behaviour, respectively. The discrepancy between the non-equilibrium and equilibrium data is particularly evident in the inner region of the boundary layer ($y/\delta < 0.15$). For example, at a similar Reynolds number of about 1200 (although different K), the difference in the values of α at $y/\delta \approx 0.07$ between the equilibrium (triangles) and non-equilibrium (diamonds and squares) data is about 16 %. This discrepancy due to non-equilibrium effects, however, does not appear to influence the turbulence statistics in the inner region of the boundary layer (see figure 14a), most likely due to the fact that the mean advection term does not play a significant role in the mean dynamics there. In the outer region ($y/\delta > 0.15$), on the other hand, mean advection dominates, and so even a small discrepancy in the value of α between the equilibrium and non-equilibrium

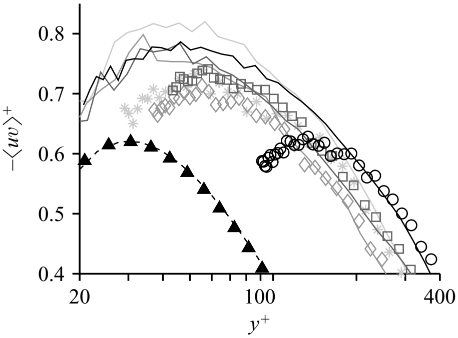

FIGURE 20. Inner normalized Reynolds stress profiles from the present data at $K = 3.7\times10^{-7}$ (open symbols and solid lines) and DNS data at $Re_\tau = 440$ (solid symbols and dotted line). The open symbols and solid lines are matched according to their greyscale, where each greyscale/symbol represents a different Re_τ, as listed in table 1. The open symbols were obtained by direct measurement from the x-array, whereas the solid lines were obtained from the u profile measurements, using the integrated mean momentum balance in (5.1). For the DNS data, the solid symbols represent $\langle uv\rangle^+$, as directly computed in the simulation, and the dashed line represents the same quantity calculated using (5.1).

data at similar Re_τ (6 % difference in α at $y/\delta \approx 0.7$) leads to noticeable effects in the turbulence statistics in the outer region (see figure 14*a*).

5.3. *Reynolds shear stress profiles*

In this section, the present experimental data are compared with two particular aspects of the multi-scale theory: (i) the location of the peak in the *modified* Reynolds stress profile, as defined in § 4.3, and (ii) the decay of the inner normalized Reynolds stress in the outer region of the boundary layer, as described in § 4.2. Direct measurements of the Reynolds stress by the x-array probe are compared to that obtained indirectly by integrating the mean momentum balance (4.1), which gives

$$\langle uv\rangle^+ = 1 - \frac{\mathrm{d}U^+}{\mathrm{d}y^+} - \epsilon^2 \int_0^{y^+} b(s)\,\mathrm{d}s. \tag{5.1}$$

The last two terms on the right-hand side of (5.1) are calculated using simultaneous data from the upstream and downstream normal-wire probes (see figure 3). The direct (x-array) and indirect (integral momentum) methods of obtaining $\langle uv\rangle^+$ are shown in figure 20 for the case of $K = 3.7\times10^{-7}$. The equilibrium DNS profile at $Re_\tau = 440$ is also displayed for comparison. With the DNS data, the direct and indirect methods yield nearly identical results across the entire boundary layer. However, for the experimental data, the two methods only agree far from the wall (approximately $y^+ > 200$ for the cases shown). Near the peak in the experimental profiles, large discrepancies exist between the two methods. Insufficient spatial resolution of the x-array probe, as well as possible interference by the probe support frame in the proximity of the wall, is believed to play a role in artificially lowering the measured $\langle uv\rangle$ values near the peak in the profile.

In the case of channel flow, one expects the peak in the Reynolds stress profile to increase with Re_τ, approaching unity as $Re_\tau \to \infty$ (Wei *et al.* 2005*a*,*b*). In the present equilibrium sink-flow data, however, the magnitude of the peak at $Re_\tau = 1646$ ($K = 3.7\times10^{-7}$, denoted by the circles in figure 20) measures 4.7 % lower than the peak at $Re_\tau = 1170$ ($K = 5.6\times10^{-7}$, data not shown). Furthermore, the peak in the equilibrium profile at $Re_\tau = 1170$ lies 7.7 % below that of the non-equilibrium data at

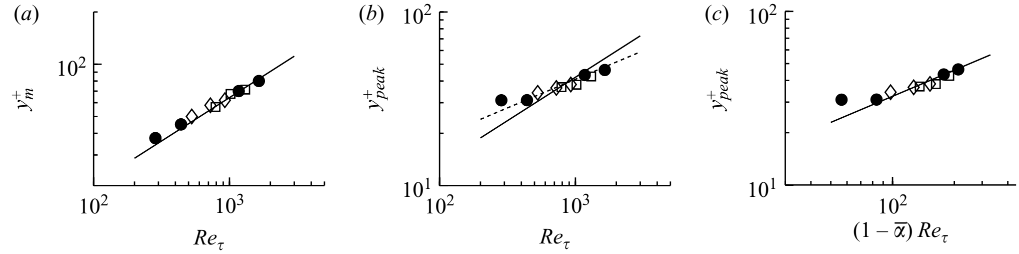

FIGURE 21. Scaling in the mesolayer: (*a*) location of peak in $\tilde{T}$ as defined in (4.4) versus Re_τ, (*b*) location of peak in $-\langle uv\rangle^+$ versus Re_τ, (*c*) location of peak in $-\langle uv\rangle^+$ versus $(1-\overline{\alpha})Re_\tau$. Solid symbols are for the equilibrium case only (combined DNS and present experimental data). Open symbols are the present non-equilibrium data: $K(\times 10^7) = 5.6$ ◇, 3.7 □. The solid black lines represent a slope of 1/2 and the dotted black line represents a slope of 1/3.

similar Re_τ (albeit different acceleration strength). Table 1 lists the inner normalized separation distance between the two wires of the x-array (d_w^+), which is the same as the active length of the individual wires (ℓ_w^+). These values range between 5.8 and 16.1 for the test cases examined here. The wire spacing normalized by the Kolmogorov length scale (estimated using the time series from the downstream normal wire in conjunction with Taylor's hypothesis and the assumption of isotropic turbulence) remained less than 5 for all values of y/δ, x/L and Re_τ (i.e. $d_w^* < 5$ in all cases). Park & Wallace (1993) show that at $y^+ \approx 30$ in a ZPG TBL with $Re_\theta \approx 2700$ (where θ denotes the momentum thickness), the magnitude of $\langle uv\rangle$ obtained from an x-array probe (having $d_w^+ = 9$) is 3 % smaller than the 'true' Reynolds stress, as measured using the nine-wire probe of Ballint, Wallace & Vukoslavcevic (1991). The study of Zhu & Antonia (1995) recommends $d_w^* = 2$–3 in order to achieve reasonable results for the Reynolds stresses. Interestingly, though, a noticeable dip occurs in the Reynolds stress profile of Zhu & Antonia (1995) (their figure 11*c*) at the location of the expected peak, despite their adherence to the criterion of $d_w^* = 2$–3. Because of this, one might overestimate the location of the peak in their data by as much as 10 viscous units, based on their x-array data alone (i.e. $y_{peak}^+ = 40$ compared to $y_{peak}^+ = 30$ as indicated by the corresponding numerical simulation). In the present study, the location of the peak measured by the x-array can be shifted by as much as 20 viscous units (and more at the highest Re_τ) compared to that indicated by the integrated mean momentum balance.

The Reynolds number dependencies of y_{peak}^+ (defined as the location of the peak in $\langle uv\rangle^+$) and y_m^+ (defined as the location of the peak in the *modified* Reynolds stress, $\tilde{T}$) are shown in figure 21, based on the indirect method of measuring $\langle uv\rangle^+$ as described above. Recall that the modified Reynolds stress was introduced in (4.4) in order to develop the proper scaling for the mean momentum balance in the mesolayer. Specifically, the multi-scale theory predicted $y_m^+ \propto (Re_\tau)^{1/2}$, assuming an x^+-independence of the mean momentum balance and, therefore, only strictly holds for the equilibrium regime. However, the same analysis may be performed for any given x^+ and an identical result obtained. Thus, the scaling properties of y_m^+ should not depend on whether the flow has reached equilibrium.

Power law relationships are indicated in figure 21 by the solid (slope = 1/2) and dashed (slope = 1/3) lines. Figure 21(*a*) reveals that all of the DNS and experimental data (both equilibrium and non-equilibrium) support the theoretical prediction that $y_m^+ \propto Re_\tau^{1/2}$. Since the *modified* Reynolds stress is not a physical quantity, though,

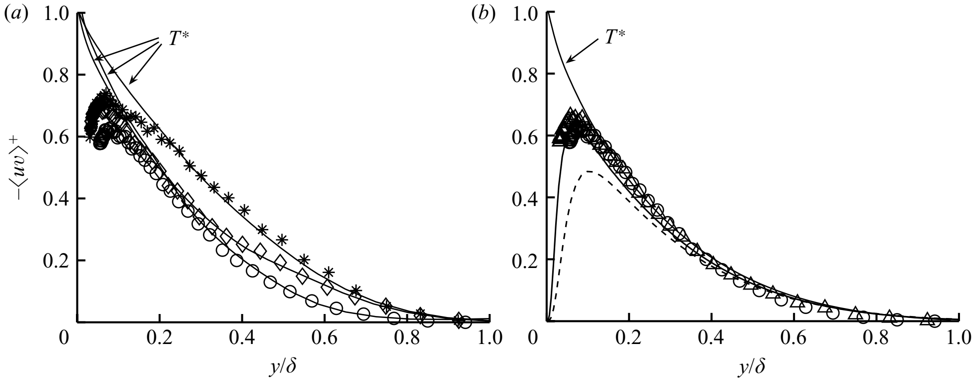

FIGURE 22. Inner normalized Reynolds stress versus y/δ showing (*a*) non-equilibrium effects at $K = 3.7 \times 10^{-7}$ and (*b*) Reynolds number effects in the equilibrium case. Symbols and lines are as in table 1. Experimental data represent the x-array measurements. The thin black lines correspond to T^* from (4.3) and were obtained by integrating the corresponding α profiles. In (*b*), T^* is based on the DNS data at $Re_\tau = 440$.

figure 21(*b*) displays the peak in the actual Reynolds stress profile as a function of Re_τ. Except for the lowest Reynolds number, all of the data indicate that $y^+_{peak} \propto Re_\tau^{1/3}$. Finally, figure 21(*c*) compares the same data versus an *adjusted* Reynolds number, i.e. $(1-\overline{\alpha})Re_\tau$. Except for the lowest Reynolds number, all of the data support $y^+_{peak} \propto [(1-\overline{\alpha})Re_\tau]^{1/2}$. An important observation is that neither the peak in the Reynolds stress profile nor the peak in the *modified* Reynolds stress profile appears to depend on the state of equilibrium of the flow and only depends on the local Reynolds number. This lends further support to the previous observation that equilibrium effects primarily influence the flow dynamics in the outer region (layer IV) only. Reynolds stress measurements in the outer region (described below) also substantiate this point.

The outer normalized Reynolds stress profiles (measured by the x-array probe) are shown in figure 22 compared to the theoretical prediction of the decay of the Reynolds stress in the outer region, T^*, as defined in (4.3). The thin black curves in the plots demonstrate this theoretical prediction for the different cases shown. In figure 22(*b*), only one theoretical curve is drawn, corresponding to the DNS data at $Re_\tau = 440$, because the T^* based on the experimental data falls directly on top of it. Importantly, $-\langle uv\rangle^+$ (symbols and thick black lines) and T^* (thin black lines) were obtained by entirely independent means, that is $-\langle uv\rangle^+$ was measured from the x-array probe, while T^* was calculated from (4.3) using measurements from the upstream and downstream normal-wire probes (see figure 3).

The theory is observed to represent the Reynolds stress extremely well in the outer region of the flow ($y/\delta > 0.15$), regardless of the equilibrium state of the flow. Closer to the wall, an exchange of balance of forces occurs, so that T^* is not expected to be an accurate representation of $\langle uv\rangle^+$ for $y/\delta < 0.15$. Figure 22(*a*) illustrates that as x/L progresses towards 0.6 (equilibrium), the magnitude of $\langle uv\rangle^+$ decreases across the entire outer region, approaching its final equilibrium profile at $x/L \approx 0.6$. The magnitude of $\langle uv\rangle^+$ decreases fastest with x/L in the wall-normal region between $0.15 < y/\delta < 0.4$ and appears to converge to the equilibrium profile slower in the region $0.5 \leqslant y/\delta \leqslant 1$. The equilibrium data (figure 22*b*) appear to be independent of Re_τ in the outer region. The significance of this observation is that the low Reynolds number DNS data may be used to predict the equilibrium behaviour at high Reynolds number, at least in the outer region in which the theoretical T^* is valid. Interestingly, Coles (1957) predicted this Reynolds-number-independent behaviour for equilibrium sink-flow TBLs half a century ago, by considering the integral momentum equation that assumes a logarithmic form of the mean velocity profile with zero wake component. Due to the lack of non-equilibrium DNS data and the limited range of Re_τ in the present experiments, it is not clear whether the same Reynolds number independence of $\langle uv\rangle^+$ in the outer region exists at every given x/L.

6. Conclusions

From a practical engineering design standpoint, there is great interest in the development of a unified framework for predicting scaling properties for large classes of different TBLs involving effects of non-equilibrium, pressure gradient, surface roughness and thermal stratification, among others. The approach described herein, based on a multi-scale analysis of the terms in the mean momentum balance, shows promise in this direction. In particular, there is no a priori assumption of a scaling structure, as used in classical overlap arguments (Millikan 1939); however, scaling patches appear naturally in the present theory from a proper rescaling of the terms in the mean momentum balance across different regions of the boundary layer. The present study serves to verify that the multi-scale approach in the previous work of Fife *et al.* (2005*b*) and Wei *et al.* (2005*a*), for canonical wall-bounded flows, also extends to TBLs with moderately Favourable pressure gradients.

One of the key features in making the extension from canonical wall flows to the FPG boundary layer is modelling the mean advection inside the boundary layer as a fraction of the pressure gradient that drives the potential flow outside the boundary layer. This allows one to recast the force balance for the FPG TBL into a form similar to that of the canonical wall-bounded flows. The main predictions from the present work are threefold: (i) intermediate scaling of the location of the peak in the Reynolds stress, (ii) the rate of decay of the Reynolds stress in the outer region and (iii) the existence of a hierarchy of scales which leads, in certain limits, to a logarithmic mean velocity profile and scaling with distance from the wall. Well-resolved hot-wire data, coupled with the previous DNS data of Spalart (1986), provided a means for evaluating the predictions of the multi-scale theory for the specific case of sink-flow TBLs (i.e. flow through a wedge). The probe configuration in the experiments allowed all of the terms in the mean momentum balance to be measured directly as functions of both the wall-normal and streamwise coordinates. In the experiments, the boundary layer was observed to be in a non-equilibrium state near the facility entrance and progressed downstream to an equilibrium state, wherein all memory of the upstream flow history had been lost, i.e. in an equilibrium state, the turbulence profiles exhibited self-similarity, at least in the outer region.

In addition to verifying the theoretical predictions listed above, the data revealed that non-equilibrium effects predominantly influence the turbulence in the outer region, whereas trends in the behaviour of the inner region turbulence are attributed solely to local Reynolds number effects, regardless of the equilibrium/non-equilibrium state of the boundary layer. The reason for the former is believed to stem from the advection term in the mean momentum balance, which requires a certain development length in order for the inertia of the outer region fluid to reach its maximum (x^+-independent) value at equilibrium. This saturation point of the mean advection appears to coincide with the location at which 'mean' entrainment of potential flow into the boundary layer ceases, analogous to the well-known situation of fully developed flow in a two-dimensional channel with parallel walls. On the other hand, since advection plays such a negligible role in the mean dynamics of the inner region, non-equilibrium effects do not significantly influence the turbulence near the wall.

The authors gratefully acknowledge the support of the Office of Naval Research (ONR) (N00014–04–1–0304; R. Joslin, grant monitor).

Appendix A. Locations of the L_β

The scaling patch locations $y_m^+(\beta)$ are determined as locations of the peaks in T_β, which in turn are derivable in terms of the actual Reynolds stress $T(y^+)$. From (4.10) and using the fact that $\mathrm{d}T_\beta/\mathrm{d}y^+=0$ at $y^+=y_m^+(\beta)$, one obtains

$$\frac{\mathrm{d}T(y_m^+(\beta))}{\mathrm{d}y^+}=\beta-\epsilon^2\,b(y_m^+(\beta)). \tag{A 1}$$

Differentiating (A 1) with respect to β gives

$$\frac{\mathrm{d}^2T(y_m^+(\beta))}{\mathrm{d}y^{+2}}\frac{\mathrm{d}y_m^+}{\mathrm{d}\beta}=1-\epsilon^2\,b'(y_m^+(\beta))\frac{\mathrm{d}y_m^+}{\mathrm{d}\beta}. \tag{A 2}$$

Also by combining (4.10), (4.13) and (4.15) gives

$$\frac{\mathrm{d}^2T(y_m^+(\beta))}{\mathrm{d}y^{+2}}=-A(\beta)\,\beta^{3/2}-\epsilon^2\,b'(y_m^+(\beta)). \tag{A 3}$$

By substituting (A 3) into (A 2) and rearranging, one finds that the β-dependent position of the peak location of each $T_\beta(y^+)$ (centred in each L_β) satisfies

$$\frac{\mathrm{d}y_m^+(\beta)}{\mathrm{d}\beta}=-\frac{1}{A(\beta)}\,\beta^{-3/2}. \tag{A 4}$$

In principle, if $A(\beta)$ were known, (A 4) could be solved to give $y_m^+(\beta)$ as a function of β, with an integration constant C. Then the relation could be inverted to obtain β as a function of $y_m^+(\beta)$ and C. Next, one would integrate (A 1), with $y_m^+(\beta)$ replaced by the symbol y^+, to get $T(y^+)$ (with a second integration constant). The last step would be to integrate (4.1) twice to obtain $U^+(y^+)$. Although $A(\beta)$ is not known explicitly, certain properties are evident and advantageous for discerning characteristics of the mean velocity and Reynolds stress profiles, as well as the locations of the patches, as described in Appendix B.

Appendix B. Scaling with distance from the wall

Information regarding the locations of the patches L_β can be learned by integrating (A 4) in an order of magnitude sense. Let $\ell(\beta)$ denote the characteristic length in the patch L_β, which will also be the order of magnitude of the width of that patch. From (4.13) and (A 4), one sees that $\ell(\beta)=O(\beta^{-1/2})$ and $\mathrm{d}y_m^+/\mathrm{d}\beta=-O(\beta^{-3/2})$. Integrating the latter reveals that ℓ is asymptotically (as $y^+\rightarrow\infty$) proportional to y^+ itself, i.e.

$$\ell\approx y^+. \tag{B 1}$$

A particular case is that of the mesolayer patch (§ 4.3), for which $\ell=O(\epsilon^{-1})$. Inverting (B 1) shows that the mesolayer is located at an inner normalized distance $O(\epsilon^{-1})$ from the wall. This is also the location of the peak in $\tilde{T}$ (4.4). Models built upon the hypothesis that length scales in the mean flow are proportional to distance from the wall have been proposed in the past (Prandtl 1925; Townsend 1976). The present method, proceeding without that hypothesis, indicates why and in what respect that proportionality rule is valid.

REFERENCES

Balint, J.-L., Wallace, J. & Vukoslavcevic, P. 1991 The velocity and vorticity vector fields of a turbulent boundary layer. Part 2. Statistical properties. *J. Fluid Mech.* **228**, 53–86.

Barenblatt, G., Chorin, A. & Prostokishin, V. 1997 Scaling laws for fully developed turbulent flow in pipes. *Appl. Mech. Rev.* **50**, 413–429.

Bradshaw, P. 1967 The turbulence structure of equilibrium boundary layers. *J. Fluid Mech.* **29**, 625–645.

Castillo, L. & George, W. 2001 Similarity analysis for turbulent boundary layer with pressure gradient: outer flow. *AIAA J.* **39**, 41–47.

Castillo, L. & Wang, X. 2004 Similarity analysis for nonequilibrium turbulent boundary layers. *J. Fluids Engng* **126**, 827–834.

Clauser, F. H. 1954 Turbulent boundary layers in adverse pressure gradients. *J. Aero. Sci.* **21**, 91–108.

Clauser, F. 1956 The turbulent boundary layer. *Adv. Appl. Mech.* **4**, 1–51.

Coles, D. 1957 Remarks on the equilibrium turbulent boundary layer. *J. Aero. Sci.* **24**, 495–506.

DeGraaff, D. & Eaton, J. 2000 Reynolds-number scaling of the flat plate turbulent boundary layer. *J. Fluid Mech.* **422**, 319–346.

Durbin, P. & Belcher, S. 1992 Scaling of adverse-pressure-gradient turbulent boundary layers. *J. Fluid Mech.* **238**, 699–722.

Erm, L. P. & Joubert, P. N. 1991 Low-Reynolds-number turbulent boundary layers. *J. Fluid Mech.* **230**, 1–44.

Falkner, V. & Skan, S. 1931 Solutions of boundary layer equations. *Phil. Mag.* **12**, 865–896.

Fife, P., Klewicki, J., McMurtry, P. & Wei, T. 2005*a* Multiscaling in the presence of indeterminacy: wall-induced turbulence. *Multiscale Mod. Sim.* **4**, 936–959.

Fife, P., Wei, T., Klewicki, J. & McMurtry, P. 2005*b* Stress gradient balance layers and scale hierarchies in wall-bounded turbulent flows. *J. Fluid Mech.* **532**, 165–189.

George, W. & Castillo, L. 1997 Zero-pressure gradient turbulent boundary layer. *Appl. Mech. Rev.* **50**, 689–729.

Hafez, S. 1991 The structure of accelerated turbulent boundary layers. PhD thesis. University of Melbourne, Australia.

Jones, W. & Launder, B. 1972 Some properties of sink-flow turbulent boundary layers. *J. Fluid Mech.* **56**, 337–351.

Jones, M., Marusic, I. & Perry, A. 2001 Evolution and structure of sink-flow turbulent boundary layers. *J. Fluid Mech.* **428**, 1–27.

Klewicki, J., Gendrich, C., Foss, J. & Falco, R. 1990 On the sign of the instantaneous spanwise vorticity component in the near-wall region of turbulent boundary layers. *Phys. Fluids* A **2**, 1497–1500.

Long, R. & Chen, T. 1981 Experimental evidence for the existence of the 'mesolayer' in turbulent systems. *J. Fluid Mech.* **105**, 19–59.

Lyons, A. 2007 Experimental study of the mean momentum balance in sink-flow turbulent boundary layers. Master's thesis, University of Utah, Salt Lake City, UT.

McKeon, B., Li, J., Jiang, W., Morrison, J. & Smits, A. 2004 Further observations on the mean velocity distribution in fully-developed pipe flow. *J. Fluid Mech.* **501**, 135–147.

Metzger, M. & Klewicki, J. 2003 Development and characterization of a probe to measure scalar transport. *Meas. Sci. Technol.* **14**, 1437–1448.

Millikan, C. 1939 A critical discussion of turbulent flows in channel and circular tubes. In *Proceedings of the Fifth International Congress of Applied Mathematics* (ed. J. Hartog & H. Peters), pp. 386–392. New York: Wiley.

Moser, R., Kim, J. & Mansour, N. 1999 Direct numerical simulation of turbulent channel flow up to $Re_\tau = 590$. *Phys. Fluids* **11**, 943–945.

Murlis, J., Tsai, H. M. & Bradshaw, P. 1982 The structure of turbulent boundary layers at low reynolds number. *J. Fluid Mech.* **122**, 13–56.

Narasimha, R. & Sreenivasan, K. 1979 Relaminarization of fluid flows. *Adv. Appl. Mech.* **19**, 221–309.

Panton, R. 1990 Scaling turbulent wall layers. *J. Fluids Engng* **112**, 425–432.

Park, S. & Wallace, J. 1993 The influence of instantaneous velocity gradients on turbulence properties measured with multi-sensor hot-wire probes. *Exps. Fluids* **16**, 17–26.

Perry, A., Marusic, I. & Jones, M. 2002 On the streamwise evolution of turbulent boundary layers in arbitrary pressure gradients. *J. Fluid Mech.* **461**, 61–91.

Perry, A., Marusic, I. & Li, J. 1994 Wall turbulence closure based on classical similarity laws and the attached eddy hypothesis. *Phys. Fluids* **6**, 1024–1035.

Piquet, J. 2001 *Turbulent Flows*. Springer-Verlag.

Pope, S. 2000 *Turbulent Flows*. Cambridge University Press.

Prandtl, L. 1925 Bericht ber untersuchungen zur ausgebildeten turbulenz. *Z. Angew. Math. Mech.* **5**, 136–139.

Rotta, J. C. 1962 Turbulent boundary layers in incompressible flow. *Prog. Aero. Sci.* **2**, 1–220.

Skare, P. E. & Krogstad, P. A. 1994 A turbulent equilibrium boundary layer near separation. *J. Fluid Mech.* **272**, 319–348.

Spalart, P. 1986 Numerical study of sink-flow boundary layers. *J. Fluid Mech.* **172**, 307–328.

Spalart, P. 1988 Direct simulation of a turbulent boundary layer up to $R_\theta = 1410$. *J. Fluid Mech.* **187**, 61–98.

Sreenivasan, K. & Sahay, A. 1997 The persistence of viscous effects in the overlap region, and the mean velocity in turbulent pipe and channel flows. In *Self-Sustaining Mechanisms of Wall Turbulence* (ed. R. Panton), pp. 253–272. Computational Mechanics Publications.

Townsend, A. 1956 *The Structure of Turbulent Shear Flow*, 1st edn. Cambridge University Press.

Townsend, A. 1961 Equilibrium layers and wall turbulence. *J. Fluid Mech.* **11**, 97–120.

Townsend, A. 1976 *The Structure of Turbulent Shear Flow*, 2nd edn. Cambridge University Press.

Wei, T., Fife, P., Klewicki, J. & McMurtry, P. 2005*a* Properties of the mean momentum balance in boundary layer, pipe, and channel flows. *J. Fluid Mech.* **522**, 303–327.

Wei, T., McMurtry, P., Klewicki, J. & Fife, P. 2005*b* Mesoscaling of Reynolds shear stress in turbulent channel and pipe flows. *AIAA J.* **43**, 2350–2353.

Wosnik, M., Castillo, L. & George, W. 2000 A theory for turbulent pipe and channel flows. *J. Fluid Mech.* **421**, 115–145.

Yaglom, A. 1979 Similarity laws for constant-pressure and pressure-gradient turbulent wall flows. *Annu. Rev. Fluid Mech.* **11**, 505–540.

Zhu, Y. & Antonia, R. 1995 Effect of wire separation on X-probe measurements in a turbulent flow. *J. Fluid Mech.* **287**, 199–223.